









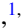




Probing the screening of the Casimir interaction with optical tweezers

L. B. Pires ^{1,2,3} D. S. Ether ^{1,2,3} B. Spreng ^{4,5} G. R. S. Araújo ⁶ R. S. Decca ⁷ R. S. Dutra ⁸ M. Borges ^{1,2,3}
F. S. S. Rosa ³ G.-L. Ingold ⁴ M. J. B. Moura ⁹ S. Frases ⁶ B. Pontes ^{1,2,10} H. M. Nussenzveig ^{1,2,3} S. Reynaud ¹¹
N. B. Viana ^{1,2,3} and P. A. Maia Neto ^{1,2,3,*}

¹LPO-COPEA, Instituto de Ciências Biomédicas, Universidade Federal do Rio de Janeiro, Rio de Janeiro, RJ 21941-902, Brazil

²CENABIO - Centro Nacional de Biologia Estrutural e Bioimagem, Universidade Federal do Rio de Janeiro, Rio de Janeiro, Rio de Janeiro 21941-902, Brazil

³Instituto de Física, Universidade Federal do Rio de Janeiro, Caixa Postal 68528, Rio de Janeiro, RJ 21941-972, Brazil

⁴Universität Augsburg, Institut für Physik, 86135 Augsburg, Germany

⁵Department of Electrical and Computer Engineering, University of California, Davis, California 95616, USA

⁶Instituto de Biofísica Carlos Chagas Filho, Rio de Janeiro, Rio de Janeiro 21941-901, Brazil

⁷Department of Physics, Indiana University-Purdue University Indianapolis, Indianapolis, Indiana 46202, USA

⁸LISComp-IFRJ, Instituto Federal de Educação, Ciência e Tecnologia, Rua Sebastião de Lacerda, Paracambi, RJ 26600-000, Brazil

⁹Departamento de Engenharia Mecânica, Pontifícia Universidade Católica do Rio de Janeiro, RJ 22451-900, Brazil

¹⁰Instituto de Ciências Biomédicas, Universidade Federal do Rio de Janeiro, Rio de Janeiro, RJ 21941-902, Brazil

¹¹Laboratoire Kastler Brossel, Sorbonne Université, CNRS, ENS-PSL Université, Collège de France, Campus Pierre et Marie Curie, 75252 Paris, France



(Received 30 March 2021; accepted 21 June 2021; published 9 July 2021)

We measure the colloidal interaction between two silica microspheres in an aqueous solution in the distance range from 0.2 to 0.5 μm with the help of optical tweezers. When employing a sample with a low salt concentration, the resulting interaction is dominated by the repulsive double-layer interaction which is fully characterized. The double-layer interaction is suppressed when adding 0.22 M of salt to our sample, thus leading to a purely attractive Casimir signal. When analyzing the experimental data for the potential energy and force, we find good agreement with theoretical results based on the scattering approach. At the distance range probed experimentally, the interaction arises mainly from the unscreened transverse magnetic contribution in the zero-frequency limit, with nonzero Matsubara frequencies providing a negligible contribution. In contrast, such unscreened contribution is not included by the standard theoretical model of the Casimir interaction in electrolyte solutions, in which the zero-frequency term is treated separately as an electrostatic fluctuational effect. As a consequence, the resulting attraction is too weak in this standard model, by approximately one order of magnitude, to explain the experimental data. Overall, our experimental results shed light on the nature of the thermal zero-frequency contribution and indicate that the Casimir attraction across polar liquids has a longer range than previously predicted.

DOI: [10.1103/PhysRevResearch.3.033037](https://doi.org/10.1103/PhysRevResearch.3.033037)

I. INTRODUCTION

The van der Waals (vdW) interaction plays a key role in several systems at the intersection between cell and molecular biology, chemistry and physics, such as biological membranes and colloids, among others [1,2]. The general theoretical framework for the vdW force was laid down by Lifshitz [3], whose work was later extended to allow for an intervening material medium between the interacting surfaces [4]. The vdW interaction across an electrolyte solution is a key ingredient of

the Derjaguin, Landau, Verwey, and Overbeek (DLVO) theory of colloidal interactions [5]. Electrodynamic retardation leads to a reduction of the contribution from nonzero Matsubara frequencies as the distance increases beyond the nanometric scale. The vdW interaction is often referred to as Casimir interaction [6] in this range, and several experiments with metallic surfaces either in vacuum [7–15] or in air [16,17] have been reported (see Refs. [18,19] for recent reviews).

In many situations of interest, the asymptotic long-distance Casimir interaction arises from the Matsubara zero frequency, which provides a purely thermal contribution proportional to the temperature T . However, when considering surfaces separated by an electrolyte solution, screening by movable ions (partly) suppresses the zero-frequency contribution over the characteristic Debye screening length [20], while leaving the contribution of nonzero frequencies unchanged [21].

The screening of the vdW interaction has been demonstrated for complex systems such as lipid bilayers [22], for

*pamn@ifufrj.br

Published by the American Physical Society under the terms of the [Creative Commons Attribution 4.0 International](https://creativecommons.org/licenses/by/4.0/) license. Further distribution of this work must maintain attribution to the author(s) and the published article's title, journal citation, and DOI.

which a direct comparison with *ab initio* theoretical models is not available. We have employed optical tweezers [23–25] to probe the interaction between silica microspheres across an aqueous solution at surface-to-surface distances $L \gtrsim 0.2 \mu\text{m}$ such that the thermal zero-frequency contribution dominates the Casimir signal. Under such conditions, the Casimir interaction is extremely sensitive to the strength of ionic screening. In addition, the simplicity of our setup allows for a direct comparison with theoretical descriptions of screening.

At such distances, the magnitude of the Casimir force between dielectric surfaces is in the femtonewton (fN) range, thus requiring the use of very soft tweezers, with a stiffness of the order of fN/nm and long measurement times. Such force sensitivity was achieved by carefully mitigating the laser and microscope stage drifts, nonthermal noises and spurious measurement signals arising from perturbations of the optical potential by the presence of the additional interacting microsphere.

A much stronger interaction is obtained by replacing dielectric surfaces by metallic ones. Experiments with different intervening liquids were implemented in the distance range close to $\sim 0.1 \mu\text{m}$ [26–30]. However, in this case the zero-frequency contribution becomes dominant only at distances above the micrometer range. Thus it would be extremely difficult to probe the screening effect with metallic surfaces. In contrast, screening is relevant already in the nanometer range when considering several examples of dielectric surfaces interacting across an aqueous medium. Indeed, in this case the zero-frequency contribution typically stands out as the dominant term already at relatively short distances, of the order of $\sim 0.1 \mu\text{m}$, due to the near index-matching at nonzero Matsubara frequencies [5,31]. For instance, the vdW interaction between lipid membranes in the nanometer range is strongly modified by changing the salt concentration and the resulting screening length [22]. Thus optical tweezers are ideally suited for probing the Casimir screening as it allows for weak trapping of dielectric particles in aqueous solution as long as the requirement of near index matching is satisfied [32], which is precisely the condition for making the zero-frequency Casimir contribution dominant in the submicrometer range.

Previously, optical tweezers were employed as force transducers to probe colloidal forces [33–39] and the nonadditivity of the critical Casimir interaction [40]. Alternatively, one can use blinking optical tweezers to control the initial distance between interacting dielectric microspheres [41–45]. Recently, femtonewton force sensitivity was achieved using an optically trapped metallic nanosphere as the probe [46]. When combined with total internal reflection microscopy (TIRM) [47], optical tweezers allow for subfemtonewton measurements [48] when reflection of the probe laser at the planar interface between the aqueous medium and the substrate is reduced [49]. Potential energy measurements of the critical [50] and electrodynamic [51–53] Casimir interactions were implemented using TIRM. Atomic force microscopy (AFM) is usually the method of choice when probing at shorter distances (see [54] for a recent review). Typically, AFM cantilevers with stiffness $\sim \text{pN/nm}$ allow to measure piconewton forces at distances in the nanometer range [55].

With the notable exceptions of Refs. [37,39], measurements with dielectric surfaces separated by distances

$\gtrsim 0.1 \mu\text{m}$ are typically made with low or intermediate salt concentrations, with the electrostatic double layer repulsive force providing a significant fraction of the total interaction. We have probed samples with low and high salt concentrations. For the latter, the electrostatic double-layer force is completely suppressed, thus allowing for a direct blind comparison between the experimental data and theoretical models for the Casimir effect. Measuring at such conditions at distances $\gtrsim 0.2 \mu\text{m}$ is challenging not only because the signal is weak, but also because the steep attractive Casimir potential leads to frequent jump-into-contact events.

We compare our experimental results with two different models of screening of the Casimir interaction. In the first one, the zero-frequency contribution is considered separately within the realm of fluctuational electrostatics taking the ions into account with the help of the linear Poisson-Boltzmann equation [56–58]. Similarly to the double-layer interaction between charged surfaces, the resulting interaction is suppressed over the screening length.

The second model is based on a recent extension [21] of the scattering approach for parallel planar surfaces [59,60] to include longitudinal channels. In contrast to the former standard model [56–58], a single formalism is applied to all Matsubara frequencies, and the zero-frequency contribution is obtained as a limit of the result for an arbitrary frequency. Movable ions in solution give rise to a nonlocal response (spatial dispersion), which in turn allows for the existence of longitudinal modes in addition to the usual transverse ones [61].

The effect of the nonlocal ionic response is shown to be negligible at nonzero Matsubara frequencies, because they are much larger than the plasma frequency associated to ions in solution [21]. As for the zero-frequency contribution, the known screened term of Refs. [56–58] is rederived as the contribution of longitudinal channels. However, an additional unscreened contribution is also obtained within the scattering model, resulting from transverse magnetic (TM) modes in the zero-frequency limit. As a result of the TM contribution, the Casimir interaction across a salt solution is predicted to be of a much longer range than previously thought, corresponding to a universal long-distance asymptotic Hamaker constant $\sim 0.9 k_B T$ in the case of parallel planar surfaces ($k_B =$ Boltzmann constant). Our experimental data at a high salt concentration allow us to check for the existence of this additional TM contribution, which is one order of magnitude larger than the contribution of nonzero frequencies in the probed distance range $L > 0.2 \mu\text{m}$.

The paper is organized as follows. Section II presents the basic ingredients for the theoretical description of the colloidal interaction between dielectric microspheres. Section III starts with a description of the experiment and then presents a detailed comparison between results and theoretical models. Section IV contains the conclusions and the final remarks. More technical aspects of the experimental methods and additional data are presented in Appendices A to E.

II. THEORY OF COLLOIDAL INTERACTIONS

Here we consider the interaction between two silica microspheres. While the probe microsphere (radius R_1) is optically

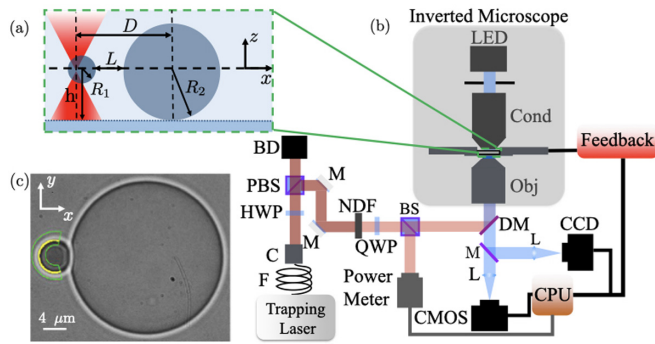


FIG. 1. (a) Sketch of two interacting silica microspheres separated by a distance L . We measure the Brownian fluctuations of the smaller one (radius R_1), which is optically trapped at a height h from the coverslip. The larger microsphere (radius R_2) is adhered to the coverslip at a distance D from the laser beam axis. (b) Experimental scheme for trapping, stabilization and position measurement: (F) optical fiber; (HWP) half-wave plate; (PBS) polarising beam splitter; (BD) beam dump; (M) dielectric mirror; (NDF) neutral density filter; (QWP) quarter-wave plate; (BS) balanced beam splitter; (DM) dichroic mirror; (L) lens; (Obj) water-immersion objective lens; (Cond) condenser lens; (CMOS) complementary metal-oxide-semiconductor camera; (CCD) charged-coupled device camera; (CPU) central processing unit. (c) A typical optical image captured by the CMOS camera. In this case, L corresponds to a few hundred nanometers. The green contour indicates the area used to detect the position of the trapped microsphere. The yellow dots are used to fit a circumference whose center represents the position. The scale bar corresponds to $4 \mu\text{m}$.

trapped, a larger one (radius R_2) is adhered to the coverslip, as illustrated by Fig. 1(a). They are separated by a surface-to-surface distance L in an aqueous solution of permittivity ϵ at temperature T . For the distance range $L \gtrsim 0.2 \mu\text{m}$ probed in our experiment, non-DLVO short-range interactions such as solvation forces are negligible [62], and the total interaction energy between the microspheres reads

$$U_{\text{int}}(L) = U_{\text{DL}}(L) + U_{\text{C}}(L), \quad (1)$$

where U_{DL} and U_{C} are the double layer and Casimir interaction energies, respectively. The Debye screening length [1,2]

$$\lambda_{\text{D}} = \sqrt{\frac{\epsilon k_{\text{B}} T}{2(Ze)^2 n_{\infty}}} \quad (2)$$

is the characteristic thickness of the ionic double layer around each particle. Here, k_{B} denotes the Boltzmann constant, Z is the ion atomic number and e is the elementary charge. The Debye length and hence the screening intensity can be controlled by changing the bulk salt concentration n_{∞} .

In the regime of long distances, the double layer around each microsphere is approximately unperturbed by the other one. Within the linear superposition approximation (LSA), the ionic charge density is then taken as the sum of separate solutions of the linear Poisson-Boltzmann (Debye-Hückel) equation for isolated microspheres [63]. Indeed, the relative difference between the LSA result and the exact solution of the linear Poisson-Boltzmann equation for two spheres

is negligibly small given our experimental conditions [64]. As charge regulation is also negligible at distances $L > \lambda_{\text{D}}$ [65,66], we consider a constant charge model, with the same fixed surface charge density σ on both silica microspheres. The resulting screened Coulomb interaction energy is then given by [67]

$$U_{\text{DL}}(L) = \frac{4\pi\sigma^2 R_1 R_2}{\epsilon \left(1 + \frac{R_1}{\lambda_{\text{D}}}\right) \left(1 + \frac{R_2}{\lambda_{\text{D}}}\right) \left(1 + \frac{L}{R_1 + R_2}\right)} e^{-L/\lambda_{\text{D}}}, \quad (3)$$

where $R_{\text{eff}} \equiv R_1 R_2 / (R_1 + R_2)$ is the effective radius.

The Casimir interaction is analyzed within the scattering approach to nontrivial geometries [68,69], which allows the derivation of exact results for the spherical geometry in terms of the corresponding Mie scattering operators [70–73] developed in the plane-wave basis [74]. Our approach also accounts for electrodynamic retardation and thermal effects. As the distance increases, deviations from the standard proximity force approximation (PFA), also known as Derjaguin approximation [75], become increasingly important [71,76–82].

The Casimir free energy is then given as a sum over the Matsubara frequencies

$$\xi_n = 2\pi n k_{\text{B}} T / \hbar, \quad n = 0, 1, 2, \dots \quad (4)$$

that reads

$$U_{\text{C}}(L) = k_{\text{B}} T \sum_{n=0}^{\infty} \log \det [1 - \mathcal{M}(\xi_n)]. \quad (5)$$

The prime stands for the multiplication by a factor $1/2$ when considering the zero-frequency ($n = 0$) contribution. The round-trip operator

$$\mathcal{M}(\xi_n) = \mathcal{T}_{12} \mathcal{R}_2 \mathcal{T}_{21} \mathcal{R}_1 \quad (6)$$

contains the reflection (Mie) operators \mathcal{R}_1 and \mathcal{R}_2 of the probe and adhered microsphere, respectively. They are calculated with respect to reference points located at their corresponding centers. The operator \mathcal{T}_{21} carries out the translation from the center of microsphere 1 to the one of microsphere 2 along the x direction. Likewise, \mathcal{T}_{12} implements the opposite translation from microsphere 2 to 1, also across the center-to-center distance $L + R_1 + R_2$, as illustrated by Fig. 1(a).

We follow Ref. [74] and develop the scattering formula (5) in the plane-wave basis with the help of a discrete Fourier transform. We take the dielectric functions of silica and water from Ref. [29]. The contribution to the medium dielectric function arising from ions in solution is considered within the Drude model, and is non-negligible only for the zero-frequency contribution.

As discussed in the previous section, the screening of the Casimir interaction by movable ions in solution is the central focus of the present paper. For the simpler geometry of planar parallel surfaces, the scattering formula for the Casimir interaction across an electrolyte solution was recently developed in terms of the nonlocal electrodynamic response of the intervening medium [21]. Only the zero-frequency contribution is modified by ions in solution, as the corresponding plasma frequency is much smaller than $k_{\text{B}} T / \hbar$. Two separate contributions were found at the zero-frequency limit: The first one, accounting for longitudinal modes, coincides with the result of previous derivations based on the linear Poisson-Boltzmann

equation [56–58]. Alongside the screened longitudinal term, the scattering approach of Ref. [21] leads to an additional, unscreened contribution arising from TM modes in the zero-frequency limit.

The main purpose of the present study is to investigate whether such additional contribution is found experimentally. We compare our data with the full Mie calculation based on the scattering formula (5) for spherical particles instead of directly applying the results of Ref. [21] or Refs. [56–58] for parallel planar surfaces. Since we probe distances $L \gg \lambda_D$, the zero-frequency contribution in (5) is completely suppressed if we follow the general scheme of Refs. [56–58]. Indeed, in this case, the zero-frequency contribution is considered separately as an electrostatic effect derived from the linear Poisson-Boltzmann equation, and then all multipole contributions are screened over the Debye length λ_D [83]. On the other hand, when taking the zero-frequency contribution as a limit of the general scattering formalism, an additional unscreened TM contribution provides the long-distance asymptotic value of the Casimir attraction, as the contribution of nonzero Matsubara frequencies becomes negligible at the distances $L \gtrsim 0.2 \mu\text{m}$ probed in our experiment. Such asymptotic result is of a universal nature as it does not depend on the details of the dielectric functions of the materials involved in the experiment [21]. In short, given our experimental conditions, the two alternative approaches amount to suppress or include the unscreened zero-frequency contribution in (5).

In the next section, we present our measurements and compare the results for the interaction energy and force with the theoretical models discussed above.

III. INTERACTION MEASUREMENTS AND COMPARISON WITH THEORETICAL MODELS

We employ a standard optical tweezers setup to probe the colloidal interactions between two silica microspheres of different radii. Figure 1 presents a sketch of the experimental setup. While the larger microsphere is adhered to the coverslip, the smaller one is optically trapped, as illustrated by panel (a). In order to align the two microsphere centers along the z axis with a precision $\delta z \sim 100 \text{ nm}$, we follow Ref. [38] and use the information from defocusing microscopy [84,85] to drive the microscope stage with our nano-positioning system. The experimental scheme is shown in panel (b), while panel (c) presents a typical optical image of the two interacting microspheres. Details regarding the experimental setup, sample preparation and characterization of the microspheres can be found in Appendices A, B, and C, respectively.

The interaction is carried out under two conditions corresponding to very different values of the Debye screening length λ_D . A specific experimental protocol is implemented to each of these two conditions, as detailed in the next two sections. We first present the methodologies which are common to both situations. We measure the position of both microspheres by applying an edge detection method [86,87], as outlined in Fig. 1(c) for the smaller microsphere (see Appendix D for details). The resulting time series $(X_1(t), Y_1(t))$ and $(X_2(t), Y_2(t))$ for the smaller and larger microsphere, re-

spectively, are the main ingredients for the analysis leading to the experimental energy and force data.

We choose a very soft transverse trap stiffness $k_x \sim 1 \text{ fN/nm}$ so as to allow for femtonewton force measurements given the nanometric precision of our position detection method (see Appendix D). A major obstacle limiting the minimum distance that we can probe is the sharp increase of the Brownian correlation time $\tau_C = \gamma/k_x$ ($\gamma =$ Stokes drag coefficient) as the distance L between the microspheres decreases for a fixed stiffness. Indeed, a longer measurement time would be needed to obtain the same amount of statistically independent values of $(X_1(t), Y_1(t))$ when probing at shorter distances. From the analysis of the position fluctuations, we measure the correlation time of the trapped particle under typical experimental conditions to be $\tau_C \sim 100 \text{ ms}$ for an average distance $\bar{L} \sim 1 \mu\text{m}$. This is in agreement with the theoretical modeling of the drag coefficient γ in the sphere-sphere geometry [88] when taking into account the Faxén correction [89] arising from the coverslip for an average height $\bar{h} \sim 12 \mu\text{m}$. We predict a fourfold increase of τ_C as the distance is reduced down to the minimum value $L \sim 0.2 \mu\text{m}$ probed in our experiment due to the variation of the drag coefficient γ [88]. At distances shorter than this minimum value, the Brownian motion becomes too slow, making it impractical to probe the potential landscape.

To overcome the challenge imposed by the large correlation time, we measure the positions over a very long time, $\mathcal{T} = 500 \text{ s}$. Such a long measurement time requires mitigation of environmental noises and drifts so as to have a thermally limited system over a time of the order of \mathcal{T} or longer. In Appendix E, we discuss the methodologies employed to render our system more stable over longer times, and how we have characterized and tested its stability. In particular, we show that our system is thermally limited at least up to a time $\approx 2\mathcal{T}$, by analyzing the Allan deviation of the position variable X_1 .

In view of the magnitude of the correlation time, we choose a sampling interval $1/f_s = 100 \text{ ms}$ ($f_s =$ sampling rate) to avoid storing correlated data, although the data become increasingly more correlated as the distance decreases. In addition, we take a short exposure time $W = 2 \text{ ms} \ll \tau_C$ to avoid the blur effect arising from Brownian fluctuations while an individual frame is captured [90]. The latter allows us to take the raw data for the position time series without introducing any model-dependent correction.

For each experimental run, 5000 frames are converted into the time series $(X_1(t), Y_1(t))$ and $(X_2(t), Y_2(t))$ while a feedback stabilization loop, shown in Fig. 1 and discussed in detail in Appendix E 2, keeps the microscope stage at a fixed position within 10 nm, which is the range of variation of $(X_2(t), Y_2(t))$. Discrete binning is then implemented for the position of the optically trapped microsphere, with a bin size of 4 nm comparable to our position resolution. As indicated by Fig. 1(a), the distance between the microspheres for a given bin i is given by

$$L^{(i)} = \bar{X}_2 - X_1^{(i)} - (R_1 + R_2), \quad (7)$$

where \bar{X}_2 corresponds to the average position of the adhered microsphere and $X_1^{(i)}$ is the position of the optically trapped one. The microsphere radius $R_1 = (2.35 \pm 0.02) \mu\text{m}$

is measured by scanning electron microscopy (SEM), with the error given by the standard deviation (see Appendix C 1). Since our batch of the large silica microspheres presented an important size dispersion, we determined their radii from the correlation of optical and SEM images, as discussed in Appendix C 2. We found $R_2 = (12.76 \pm 0.06) \mu\text{m}$ and $R_2 = (11.74 \pm 0.06) \mu\text{m}$ for the microspheres used with low (Sec. III A) and high (Sec. III B) salt concentrations, respectively. While the error of the center-to-center distance $\bar{X}_2 - X_1^{(i)}$ is in the nanometer range, the global offset arising from the subtraction of $R_1 + R_2$ has a higher error which is not written explicitly as it does not change the relative values of $L^{(i)}$.

The binned data for each experimental run lead to a frequency histogram from which we obtain the probability distribution $p(L^{(i)})$. Since our system remains in thermal equilibrium over a time scale longer than the total measurement time \mathcal{T} , we associate $p(L^{(i)})$ to a Boltzmann distribution [40,91] at the measured temperature $T = (296 \pm 1)$ K. For each salt concentration, we choose a reference distance L_{ref} with a high number of occurrences for all different runs so as to be able to accurately determine $p(L_{\text{ref}})$ from the available data. We then infer the total potential energy $U(L^{(i)})$ from

$$U(L^{(i)}) - U(L_{\text{ref}}) = -k_B T [\log p(L^{(i)}) - \log p(L_{\text{ref}})], \quad (8)$$

where k_B is the Boltzmann constant.

Equation (8) determines the potential energy from the probability distribution $p(L^{(i)})$ apart from an arbitrary offset as expected on physical grounds. After subtracting the optical potential $U_{\text{opt}}(L^{(i)})$, which, as discussed below, is determined by measurements when the two microspheres are sufficiently apart, we average the results for the interaction energy $U_{\text{int}}(L^{(i)}) = U(L^{(i)}) - U_{\text{opt}}(L^{(i)})$ from different runs. From now on, we will omit the bin index i .

In addition to the environmental noise discussed in detail in Appendix E, one important concern is the modification of the optical force as the adhered microsphere is brought closer to the laser focal spot. We expect the reverberation of the laser beam between the interacting microspheres to be negligible since their refractive index $n_{\text{bead}} = 1.4146$ is close to the refractive index of the host medium $n_{\text{water}} = 1.3242$ (see Appendix E 3 for details). Indeed, the corresponding Fresnel reflectivity is as small as 0.1% for normal incidence. In addition, the optical reverberation between the trapped particle and the coverslip [92] is unimportant in our experiment as the former is kept at a fixed height with respect to the latter.

Yet optical perturbations might still be present as part of the trapping beam is refracted through the adhered microsphere before reaching the focal plane. In contrast to the reverberation effect, such perturbation does not involve interference and is thus expected to depend only on the relative refractive index and the geometrical aspect ratio D/R_2 , where D is the distance between the (unperturbed) focal point lying along the optical symmetry axis and the center of the adhered sphere as indicated in Fig. 1(a). Preliminary theoretical results [93] indicate a total displacement of the optical equilibrium position along the x axis of a few tens of nanometers and a variation of stiffness of a few percent as the adhered sphere is brought from infinity to a distance of closest approach of a few hundred nanometers.

In view of the above results, we measure the optical equilibrium position $X_{1,\text{eq}}^{\text{opt}}$ and the trap stiffnesses k_x and k_y (see Appendix E 2), characterizing the optical potential $U_{\text{opt}}(L)$, at intermediate distances D such that the surface-to-surface distance at optical equilibrium $L_{\text{eq}}^{\text{opt}}$ lies in the interval from 480 nm to 800 nm. In this range, colloidal interactions in our system are negligible and then $X_{1,\text{eq}}^{\text{opt}}$ is obtained from the average position. More importantly, our calibration of the optical equilibrium position already takes the beam perturbation into account. As the geometrical aspect ratio D/R_2 changes by only $\sim 2.5\%$ within this interval, we expect the optical potential to be approximately independent of D . We have verified, experimentally, that k_x , k_y , and $X_{1,\text{eq}}^{\text{opt}}$ (see Appendix E 1) are indeed independent of D within the experimental error in this range of distances.

In order to push further into the interaction region, we reduce the distance D between the adhered sphere and the optical symmetry axis by up to ~ 150 nm with respect to the smallest value of D employed when characterizing the optical potential. We assume that $X_{1,\text{eq}}^{\text{opt}}$ and k_x are still constant in this case. This is verified by measuring k_y (see Appendix E 3), while the total stiffness $k_x - \partial_x F_{\text{int}}$ and the equilibrium position change due to the colloidal interactions. To further verify that our interaction measurements are not contaminated by perturbations of the optical force, we perform measurements at different laser powers, as discussed in the next section.

A. Low salt concentration

In this section, we present the results for the colloidal interaction and discuss some additional experimental details which are specific to the experiment with no added salt. In this case, the double-layer force is dominant and the total force is repulsive over the entire probed range of distances. In order to overcome the repulsive interaction and adhere the larger microsphere to the coverslip as indicated in Fig. 1(a), we coated the latter with poly-L-lysine (see Appendix C 1).

We performed 25 interaction runs for the same pair of microspheres, each run corresponding to fixed values for the distance D and the laser power. We employed three different values for D and several values for the laser power, with the resulting k_x ranging from 1.2 to 2.5 fN/nm [see Fig. 8(a) of Appendix E for details]. In addition, we performed four calibration measurements, employing a larger distance D , in order to determine the optical equilibrium position $X_{1,\text{eq}}^{\text{opt}}$, which was such as to correspond to a surface-to-surface separation $L_{\text{eq}}^{\text{opt}} = 480$ nm. After subtracting the optical potential $U_{\text{opt}}(L)$ from the total potential energy $U(L)$, we find no systematic effect of the laser power on the measured interaction energy, as the data for $U_{\text{int}}(L)$ coming from different runs are compatible with each other and do not split according to the laser power. Indeed, any additional perturbation of the optical potential as the adhered microsphere is brought closer to the trapped one would result in the contamination of $U_{\text{int}}(L)$ by a residual optical potential proportional to the laser power after subtraction of the unperturbed optical potential. Thus our analysis indicates that such additional perturbation is negligible when compared to our experimental sensitivity.

We average the data for $U_{\text{int}}(L)$ from the 25 runs, combining different laser powers and values of D , and plot the

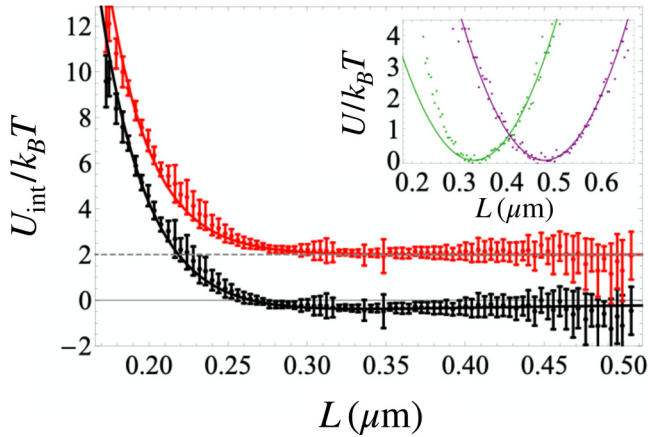


FIG. 2. Interaction energy in units of $k_B T$ versus distance for the sample with a low salt concentration: experiment (points with error bars representing the standard error of the mean), and theoretical fits based on two different theoretical models of the Casimir interaction, either with (black) or without (red) the unscreened contribution from TM modes in the limit of zero frequency. The latter is displaced by $2k_B T$ and the same experimental data is plotted twice for better visualization. For both models, the double-layer repulsive interaction is calculated within the linear superposition approximation in terms of two fitting parameters: the squared charge density σ^2 and the Debye screening length λ_D . In the inset, we plot the total energy versus distance for two individual runs. The purple and green plots correspond to the adhered microsphere placed further and closer to the laser beam axis, respectively. In both plots, the solid line represents the optical potential.

results in Fig. 2. The error bars represent the standard error of the mean of the combined set of data and the common reference distance is $L_{\text{ref}} = 0.27 \mu\text{m}$ [94]. For the purpose of illustrating how those results are obtained, we also plot the total energy $U(L)$ corresponding to two individual runs in the inset. While the purple points correspond to the calibration configuration used to characterize $U_{\text{opt}}(L)$, the green ones represent a single interaction run with a smaller D and the same laser power taken here as a typical example. We determine the optical equilibrium position $X_{1,\text{eq}}^{\text{opt}}$ as the position average given the probability distribution corresponding to the purple points (no interaction). The surface-to-surface optical equilibrium position $L_{\text{eq}}^{\text{opt}} = 480 \text{ nm}$ is then obtained from $X_{1,\text{eq}}^{\text{opt}}$ by using Eq. (7). The optical stiffness k_x is derived from the experimental calibration methods described in Appendix E 3. The resulting optical potential $U_{\text{opt}}(L) = k_x(L - L_{\text{eq}}^{\text{opt}})^2/2$ is represented by the solid purple curve, which is also a good quadratic fit of the purple points as expected. Finally, the green solid curve is the optical potential with the same stiffness and $X_{1,\text{eq}}^{\text{opt}}$ but with a different value of $L_{\text{eq}}^{\text{opt}}$ as determined by Eq. (7), since it corresponds to a smaller value \bar{X}_2 for the position of the adhered microsphere. The resulting displaced curve represents the optical potential $U_{\text{opt}}(L)$ in the interaction run taken as example. When compared to the experimental curve for $U(L)$ (green points), it makes more apparent the skewness of the latter, which indicates the repulsive nature of the colloidal interaction. Finally, the data for $U_{\text{int}}(L)$ coming

TABLE I. Parameters employed for the curve fit of the measured interaction energy: charge density σ and Debye screening length λ_D . In addition to the double-layer interaction energy (3), we also consider the Casimir interaction either with or without the zero-frequency TM contribution.

Casimir model	σ (mC/m ²)	λ_D (nm)
$n = 1, 2, \dots$	-1.7 ± 0.3	25.0 ± 0.9
$n = 0, 1, 2, \dots$	-0.8 ± 0.1	29.3 ± 0.6

from this specific run is then the difference between the green points and the green solid curve shown in the inset.

In order to allow for comparison with two distinct theoretical models of Casimir screening, we plot in Fig. 2 the same experimental results for $U_{\text{int}}(L)$ twice for better visualization, with the red points shifted by $2k_B T$ with respect to the black ones. The curve fits are then based on two distinct models of the Casimir attractive interaction, either with (black) or without (red) the contribution arising from TM channels in the zero-frequency limit (see Sec. II for details). In both cases, the double-layer repulsive interaction is calculated within the LSA and obtained from Eq. (3) in terms of two fitting parameters: the squared charge density σ^2 and the Debye screening length λ_D . We fit over the interval $L_{\text{min}} \leq L \leq 440 \text{ nm}$ and take values for L_{min} between 190 and 210 nm. We also consider different data sets obtained by changing the reference distance L_{ref} by a few tens of nanometers (not shown in the plot). In Table I, we show the average of the fitted values of σ and λ_D with the errors representing the standard deviation.

The red curve in Fig. 2 corresponds to a repulsive colloidal potential over the entire range of distances probed in our experiment. On the other hand, the black solid line exhibits a very weak attraction for distances $L \gtrsim 0.35 \mu\text{m}$, since in this range the TM zero-frequency contribution is much larger than the combined contribution of all nonzero Matsubara frequencies. However, such smooth variation is below our experimental sensitivity. Thus both models fit our data equally well, although the fitting parameters are more stable with respect to the fitting range when the zero-frequency TM contribution is included, as indicated by the standard deviations shown in Table I.

The results for λ_D shown in Table I differ by merely $\sim 20\%$. They correspond to a salt concentration $n_\infty \sim 0.2 \text{ mM}$, which is compatible with sample contaminations arising, for instance, from the poly-L-lysine coating employed to adhere the larger microsphere to the coverslip. The slightly larger value of λ_D obtained when including the zero-frequency TM contribution is required to yield a double-layer repulsion with a longer range that compensates for the stronger Casimir attraction in this case (see Sec. III B). As indicated in Table I, the corresponding charge density σ is then lowered by a factor ~ 2 in order to also fit at shorter distances. We conclude that the fitted value of σ depends strongly on the theoretical model of the Casimir interaction even in the distance range $L > 0.1 \mu\text{m}$ where it is clearly subdominant. Model-dependent results for colloidal parameters were also reported in Ref. [52].

Usually, the surface charge density is obtained by fitting the interaction force at much shorter distances, $L \lesssim$

20 nm, by considering a Casimir (vdW) model without the zero-frequency TM contribution. Available results for the silica charge density for several symmetric inorganic salts at ~ 0.2 mM tend to cluster, for a pH = 5.6, at $\sigma \sim -4$ mC/m² [54]. Since the magnitude of the silica charge density increases with an increasing pH [95], the discrepancy with respect to the values shown in Table I cannot be attributed to the higher pH of our sample (pH = 6.8). Theoretical modeling of silica charging [95] seems to favor the values shown in Table I, and especially the one found when including the TM zero-frequency contribution.

The two models of Casimir screening can hardly be distinguished in experiments with low salt concentrations, since the Casimir interaction is sub-dominant over the entire distance range probed experimentally. In order to isolate the Casimir interaction from the electrostatic double-layer signal, we performed an experiment with a much higher salt concentration as presented in the next section.

B. High salt concentration

When the double-layer interaction is totally suppressed by ionic screening, the force signal at distances $L \gtrsim 0.2 \mu\text{m}$ is considerably weaker, making it harder to measure. Moreover, the equilibrium position of the probe particle becomes more unstable, due to the sharp increase of the attractive Casimir force at short distances. Experimentally, it is difficult to control the distance D between the adhered microsphere and the laser beam so as to hit the narrow range of distances in which the Casimir attraction is measurable and yet not strong enough to make the probe jump into contact in the beginning of the run.

We prepare a sample with a NaI concentration of $n_\infty = 0.22$ M, corresponding to $\lambda_D = 0.64$ nm according to Eq. (2). Such value for the Debye screening length is sufficiently small to produce a complete suppression of the double-layer interaction for $L \gtrsim 0.2 \mu\text{m}$. The interaction runs are performed for average separations of the order of $\bar{L} \sim 0.4 \mu\text{m}$. To determine the parameters of the optical potential alone, we take 8 different average separations in the range $0.5 \mu\text{m} < \bar{L} < 0.9 \mu\text{m}$. Those calibration measurements are repeated before and after every two interaction measurements. In all cases, we find variations of the optical equilibrium position and trap stiffnesses k_x and k_y comparable to the corresponding experimental errors. The laser drift is negligible during each run and also from one run to the next, as discussed in Appendix E 1. In order to combine all interaction runs, we take $L_{\text{ref}} = 455$ nm as the reference separation. All measurements are performed with the same laser power.

We subtract the optical potential from the total potential and plot the resulting Casimir energy versus distance in Fig. 3. We compare the experimental data (points) with the two different screening models for the Casimir interaction: with (black solid line) and without (red solid line) the unscreened contribution from TM modes in the limit of zero frequency. No fitting procedure is implemented here, as the theoretical Casimir energy is obtained exclusively from the known dielectric functions of silica and water [29]. Because of the near index-matching between silica and water at nonzero Matsubara frequencies, the standard procedure [58] of disregarding

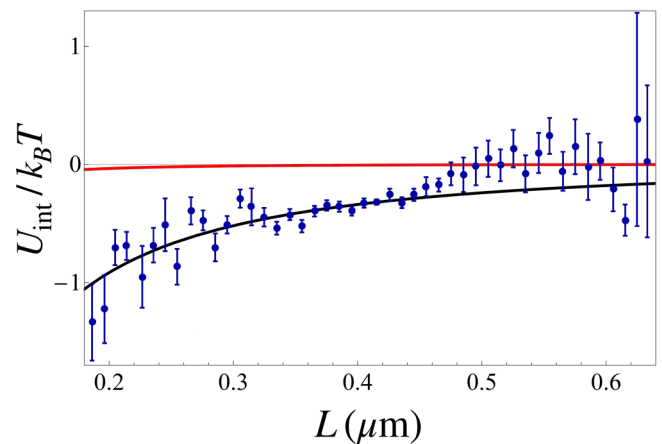


FIG. 3. Casimir energy in units of $k_B T$ versus distance for the sample with a high salt concentration: experiment (points with error bars representing the standard error of the mean) and theory either with (black) or without (red) the unscreened contribution from TM modes in the limit of zero frequency. The salt concentration of $n_\infty = 0.22$ M, corresponding to a screening length $\lambda_D = 0.64$ nm, is such that the double-layer interaction is completely suppressed in the distance range probed experimentally.

TM scattering channels in the zero-frequency limit leads to a negligibly small interaction energy, which cannot explain our data as indicated in Fig. 3, even if one takes the distance offset as a fitting parameter. On the other hand, a blind comparison with the full scattering theory shows a good agreement with the experimental data.

In addition to the interaction energy, we also probe the interaction force $F_{\text{int}} = k_x (L_{\text{eq}}^{\text{int}} - L_{\text{eq}}^{\text{opt}})$, with negative sign denoting attraction, by measuring the equilibrium distance $L_{\text{eq}}^{\text{int}}$. The equilibrium distance does not necessarily coincide with the average distance \bar{L} because the probability distribution $p(L)$ has a negative skewness that results from the nonlinear Casimir attraction. More specifically, using a quadratic polynomial to fit the potential $U(L)$ overestimates the magnitude of the force as $\bar{L} < L_{\text{eq}}^{\text{int}}$ in the case of negative skew. Thus we determine $L_{\text{eq}}^{\text{int}}$ by fitting the potential with a cubic polynomial when considering experimental runs corresponding to asymmetric probability distributions. On the other hand, using the cubic polynomial for the runs with the largest values of D leads to overfitting. Indeed, the potential is expected to be approximately quadratic as the interaction is negligible when the adhered microsphere is placed far from the laser beam. We use the absolute value of the skewness $|\mu_3| \equiv |[(L^{(i)} - \bar{L})/\sigma_x]^3|$ ($\sigma_x =$ standard deviation) of the probability distribution for each experimental run (corresponding to a fixed distance D) to define which polynomial degree is taken in the fitting procedure: quadratic for $|\mu_3| \leq 0.05$, and cubic otherwise. All measured values of μ_3 are compatible with theoretical predictions for the second derivative of the Casimir force provided that the TM zero-frequency contribution is included.

In Fig. 4, we plot the interaction force as a function of the separation distance $L = L_{\text{eq}}^{\text{int}}$ in equilibrium. In contrast with the potential energy plots of Figs. 2 and 3, here each data point is the result of a fit of the entire potential obtained from a given run corresponding to a fixed value of D . The shaded

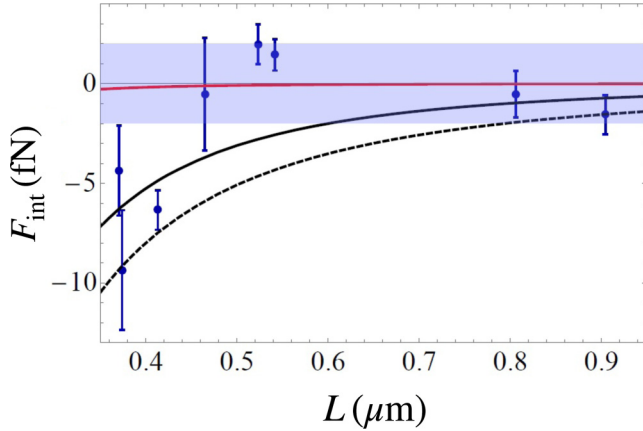


FIG. 4. Casimir force versus distance: experiment (points with error bars) and theory either with (black) or without (red) the unscreened contribution from TM modes in the limit of zero frequency. The dashed curve corresponds to the proximity force approximation with TM zero-frequency modes included. The light blue band indicates the experimental sensitivity for force measurements in our setup.

area indicates the sensitivity 2 fN of our force measurement, which is determined by the error of the equilibrium position as discussed in Appendix E 1. As in the case of the Casimir potential shown in Fig. 3, we find agreement only with the theoretical prediction including the contribution of TM channels in the zero-frequency limit (solid black line). The contribution of nonzero Matsubara frequencies (red) is smaller by about one order of magnitude and cannot describe our data. Previous experiments under similar conditions [37,39] also found a signal larger than predicted by the standard theoretical model that excludes TM modes in the zero-frequency limit.

We also plot the theoretical results (dashed) obtained by considering the spherical geometry within PFA [75], with the TM zero-frequency contribution included. The PFA provides a direct connection between the spherical geometry and the parallel-planes one considered in Ref. [21] and is asymptotically valid for large aspect ratios $R_{\text{eff}}/L \gg 1$ [96]. Although PFA overestimates the exact Mie scattering results for the force by $\sim 50\%$ for the parameters corresponding to Fig. 4, our data do not allow for a discrimination between the two theoretical models that include the TM channels in the zero-frequency limit.

IV. CONCLUSION

We developed a protocol for using optical tweezers to measure the surface interaction between silica microspheres separated by distances above $0.2 \mu\text{m}$ in aqueous solution. For the sample with the highest salt concentration, the measured potential energy corresponds to an attractive Casimir force in the femtonewton range. We find good agreement (no fitting) between our experimental data and the scattering theory which contains the unscreened contribution of transverse magnetic modes in the zero-frequency limit. Such contribution dominates the total Casimir signal by roughly one order of magnitude and is not included in the standard description of the van der Waals interaction across ionic solutions.

When measuring the surface interaction at lower salt concentrations, the theoretical description of the Casimir effect has an impact on the characterization of the repulsive double-layer interaction, particularly on the fitted value for the surface charge density.

The higher salt concentration employed in the Casimir experiment is comparable to typical values found in living cells [97]. Thus the indication that the Casimir interaction is stronger and of a longer range under such conditions might have important implications in the fields of cell and molecular biology.

ACKNOWLEDGMENTS

We thank Tanja Schoger for sharing preliminary theoretical results on the perturbation of the optical force by the presence of an additional microsphere. We also thank Antoine Canaguier-Durand, Sergio Ciliberto, Anne Le Cunuder, Arne Gennerich, Romain Guérout, Astrid Lambrecht, Umar Mohideen, Jeremy Munday, George Palasantzas, Rudolf Podgornik, and Vitaly Svetovoy for enlightening discussions. We acknowledge funding from the Brazilian agencies Conselho Nacional de Desenvolvimento Científico e Tecnológico (CNPq–Brazil), Coordenação de Aperfeiçoamento de Pessoal de Nível Superior (CAPES–Brazil), Instituto Nacional de Ciência e Tecnologia Fluidos Complexos (INCT-FCx), and the Research Foundations of the States of Minas Gerais (FAPEMIG), Rio de Janeiro (FAPERJ) and São Paulo (FAPESP). This work was also supported by Centre National de la Recherche Scientifique (CNRS), Sorbonne Université, and Deutscher Akademischer Austauschdienst (DAAD) through their collaboration programs Projet International de Coopération Scientifique (PICS), Convergence International, and PROBRAL, respectively. We are grateful to the Instituto Nacional de Metrologia, Qualidade e Tecnologia (Inmetro) for letting us use their high-resolution scanning electron microscope.

APPENDIX A: EXPERIMENTAL SETUP

A schematic of our experiment is shown in Fig. 1(b) of the main text. A 1064 nm laser beam (YLR-5-1064LP, IPG Photonics) exits an optical fiber and is divided using a half wave plate and a polarized beam splitter. While the transmitted laser light is blocked, the reflected one is directed towards alignment mirrors, an attenuation neutral density filter, and a quarter-wave plate, fitted to change the laser beam well-defined linear polarization into circular polarization. In fact, this procedure is important in order to produce equal optical trap stiffnesses along the x and y axes in the plane orthogonal to the beam propagation axis z . The laser beam is then divided again by a balanced nonpolarized beam splitter, which halves the light into a power meter (1936C and 918D-UV-OD3R, Newport) and towards the microscope (Eclipse Ti-S, Nikon). Under the microscope, the laser beam hits a dichroic mirror (ZT532rdc-NIR-R725-1100-UF2, Chroma) with high reflectance for 1064 nm and high transmittance for visible light.

A $60\times$ water-immersion objective (CFI60 Plan Apochromat VC, Nikon) with a numerical aperture of $NA = 1.2$

focuses the laser light on the sample. The objective corrects the spherical aberration introduced by the index mismatch at the glass-water interface, then allowing reliable optical trapping and imaging at heights of dozens of micrometers above the coverslip. In comparison with oil-immersion objectives, water-immersion also requires shorter stabilization times, as water is less viscous than common immersion oils, consequently decreasing systematic errors associated with image drifts.

For brightfield illumination, we used a 470-nm wavelength light produced by a high-power mounted LED (M470L3, Thorlabs), chosen to also avoid heating effects in the sample. After passing through a $NA = 0.85$ condenser lens, the light traverses the sample and is gathered by the objective lens. Transmitted afterwards by the dichroic mirror, the light is then recollected by the tube lens and directed into a CMOS (Orca-flash 2.8, C11440-10C, Hamamatsu) camera for measurements and visualization, and into a CCD camera for active feedback stabilization. The displacements in the sample are controlled by a digital piezoelectric controller (E710, Physik Instrumente) connected to the microscope stage, in which the sample chamber is attached. All the optical elements are mounted on an optical breadboard (M-SG-30x60-4, Newport), placed on a conventional optical table (RS-2000 Newport).

APPENDIX B: SAMPLE PREPARATION

Our sample is composed of a dispersion of two sets of uncoated silica microspheres with nominal manufactured radii of $\bar{R}_1 = 2.5 \mu\text{m}$ (Cat#24332, Polysciences, Inc.) and $\bar{R}_2 = 10 \mu\text{m}$ (DNG-B020, DiagNanoTM) diluted in an ultra-pure water solution (Millipore). A 1:1 salt (Sodium Iodate, Scientific NaI-Exodus) is added in the case of high salt concentration measurements. The prepared solution is then introduced inside the sample chamber composed of a rubber O-ring between two cleaned coverslips ($24 \text{ mm} \times 60 \text{ mm}$ and $24 \text{ mm} \times 32 \text{ mm}$, Knittel Glass) and properly sealed with silicone grease. For the calibration runs, the sample temperature is monitored by a thermocouple (5TC-TT-T-30-36, Omega) immersed in solution and connected to a thermometer (DP24-T, Omega). Over the range of laser powers ($\sim \text{mW}$) used in the interaction and calibration experiments, the temperature is given by $T = (296 \pm 1) \text{ K}$ and no changes are observed.

APPENDIX C: CHARACTERIZATION OF MICROSPHERES

1. Scanning electron microscopy (SEM)

Knowing the radii of the microspheres is crucial to determine the distance offset from the relation $L = \bar{X}_2 - X_1 - (R_1 + R_2)$ [see Figs. 1(a) and 1(c)]. To perform this task, high resolution scanning electron microscopy (SEM) is applied on test samples containing separately one of the two sets of silica microspheres. A glass coverslip (Paul Marienfeld GmbH & Co. KG, Germany) previously coated with 0.01% poly-L-lysine (Sigma-Aldrich, Darmstadt, Germany) and containing the targeted microspheres is firstly fixed upon a metallic SEM stub using a conductive carbon tape (Pelco TabsTM, Stansted, Essex, UK). The glass coverslip is then dried with a weak jet

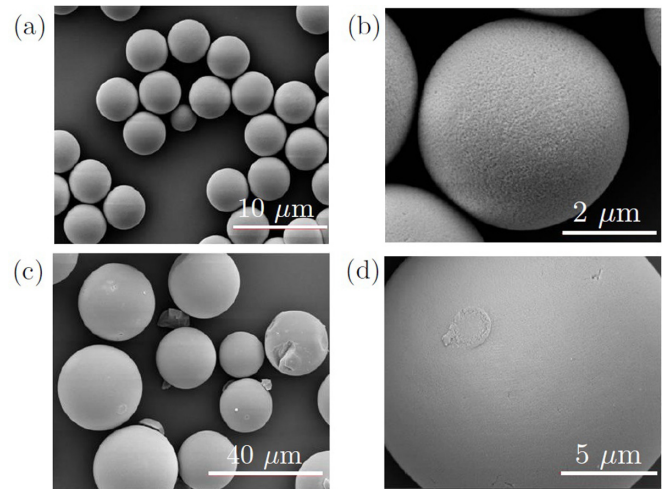


FIG. 5. Typical SEM images for characterization of the silica microspheres employed in our measurements. (a), (b) and (c), (d) correspond to batches with nominal radii $\bar{R}_1 = 2.5 \mu\text{m}$ and $\bar{R}_2 = 10 \mu\text{m}$, respectively. Scale bars are shown in each panel.

of nitrogen gas to avoid contamination, and afterwards coated with a 4–5 nm thick platinum layer using a sputtering device (Leica EM SCD 500, Wetzlar, Germany). Finally, the sample is characterized using a scanning electron microscope (Quanta 450TM FEG, FEI Company, USA) operating at 5 kV.

Typical SEM images are shown in Fig. 5. Panels (a) and (b) correspond to the set of small silica microspheres, while (c) and (d) show images from the set of large ones. Figure 5(a) shows that the first group exhibits a small size dispersion, with radius of $R_1 = (2.35 \pm 0.02) \mu\text{m}$. The standard deviation is calculated from the analysis of 10 microspheres. In contrast to the first group, the batch of large microspheres displays a much wider size dispersion, as illustrated by Fig. 5(c). Thus for this group we cannot infer the radii of the specific microspheres employed in the interaction measurements directly from the SEM ensemble characterization. We follow instead the correlative microscopy procedure [98,99] outlined in the next section.

Although SEM is not the optimal technique for surface roughness characterization, it is worthwhile to estimate the two length scales controlling the magnitude of the roughness correction to the Casimir interaction [51,100–105]: the transverse correlation length ℓ_C and the rms roughness amplitude a . The effect of roughness of silica particles is extremely important when probing shorter distances, $L \lesssim 10 \text{ nm}$ [55,106]. From images like the one shown in Fig. 5(b), we estimate $\ell_C < 50 \text{ nm}$ and $a \lesssim 10 \text{ nm}$ for the first set of microspheres, with the highest spikes in the range close to $\sim 100 \text{ nm}$. Since the roughness correction to the Casimir interaction typically scales as $(a/L)^2$ [107–109], we expect corrections $\sim 1\%$ or smaller over the distance range probed in our experiment, also because the condition $\ell_C < L$ reduces the corrections even further [110–113]. Although the presence of long spikes might produce additional roughness corrections beyond the perturbation regime [114,115], they have been neglected when modeling the Casimir interaction given that our precision is at the level of $\sim 10\%$. In addition, the good agreement with our

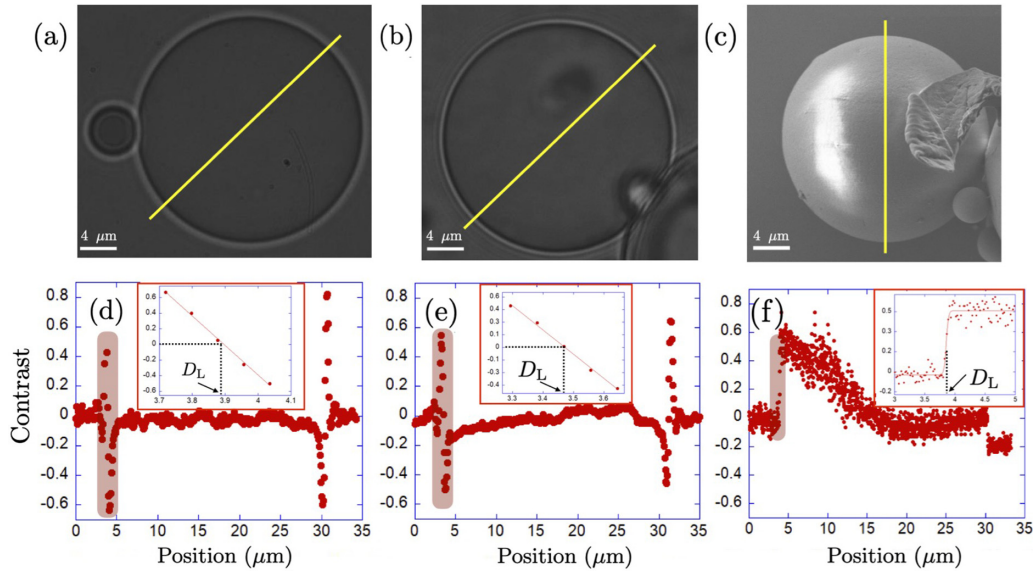


FIG. 6. Optical images of the (a) microspheres employed in the interaction measurement and (b) taken as a reference for the method of correlative microscopy. The SEM image of the same reference microsphere (b) is shown in (c). Each image is analyzed in terms of the grey level contrast along the diameters indicated by yellow lines. [(d)–(f)] Contrast vs position for each corresponding image shown on the top line. The edge regions (light red) are zoomed in the insets. The edge positions D_L are then determined by appropriate fits (see text for details).

data indicates that roughness does not play a major role in our experiment.

Overall, the surfaces of the microspheres from the second set look more smooth in the SEM images. However, they present defects in the form of protrusions and depressions, as shown in Fig. 5(c). As they are big enough to be visible in the optical microscope, they can be avoided during the experimental runs.

2. Correlative microscopy

Since it is not possible to carry out SEM on the specific large microsphere used in the experiment, a reliable measurement of its radius is achieved by correlative microscopy [98,99]. In a nutshell, this technique consists of inferring the radius of that specific microsphere by correlating optical and SEM images of microspheres from a different sample. Figure 6(a) shows the optical image of the two microspheres employed in the measurement with low salt concentration. Similar images are obtained for the pair of microspheres used in the experiment with added salt. Since the size dispersion of the set of small microspheres is negligible, we focus on the image of the large one. We prepare a sample from the set of large microspheres and tag one specific microsphere whose optical image, shown in Fig. 6(b), is similar to the image of the probed one. In addition, we displace the microscope stage along the z axis until its optical image resembles more closely the image 6(a) corresponding to the measurement run. The same microsphere shown in Fig. 6(b) is then analyzed with SEM and the resulting image is shown in Fig. 6(c). In Figs. 6(d)–6(f), we plot the contrast $C = I/I_0 - 1$ measured along the straight (yellow) lines along the microsphere diameter shown in panels (a)–(c). They are calculated for each corresponding image shown on top. Here, I and I_0 are the

grey levels at a given image point and at the background, respectively.

Figure 6(d) shows that the contrast vanishes across the central region and then displays a sharp variation at the microsphere edge, which is blurred by diffraction. We define the optical edge as the point where the contrast vanishes inside the edge region highlighted in light red. The inset is a zoom illustrating the determination of the optical edge coordinate D_L on the lefthand side by a linear fit. Such point is not an indication of the actual physical edge [85]. Nevertheless, it is a useful reference that can be measured with an excellent precision from the variation of the contrast. The same procedure is implemented in Fig. 6(e) for the optical image of the tagged microsphere to be compared with the SEM image. In both cases, the optical radius is defined as $R_{\text{opt}} = \frac{1}{2}(D_R - D_L)$, where D_R is the coordinate of the optical edge on the opposite side of the image.

The key requirement in correlative microscopy is to produce a SEM image of the same microsphere that was optically imaged in Fig. 6(b). A rectangular mark made in the central region of the coverslip with a diamond-tipped pen is used as a reference to identify each single microsphere, and in particular the one selected for the optical image Fig. 6(b). After capturing the optical image, the preparation for SEM is implemented as described in Appendix C 1.

The next step is to analyze the SEM image of the tagged microsphere. As shown in Fig. 6(c), the edge of each microsphere is sharp and not blurred by diffraction. Thus it is possible to directly access the physical radius R_2 from the SEM image. We fit a hyperbolic tangent function to the contrast function plotted in Fig. 6(f). The inset is a zoom of the edge region revealing the edge position D_L as derived from SEM. The physical radius R_2 is then determined from D_L and the position of the opposite edge located across the microsphere diameter.

The final step consists of correlating the optical and SEM images of the same microsphere in order to derive the scale factor $r_c = R_{\text{opt}}/R_2$. The entire procedure is repeated for three distinct tagged microspheres. After averaging the results, we find $r_c = 1.041 \pm 0.005$, where the uncertainty corresponds to the standard error of the mean. Knowing r_c , the physical radius R_2 of a particular microsphere in interaction can be directly inferred by measuring the corresponding optical radius R_{opt} . The results for the microspheres employed in the measurement runs are indicated in Sec. III.

3. Distance upon contact

When performing the experiment with high salt concentration, in most experimental runs we observed that the probed particle eventually jumps into contact with the adhered microsphere. By measuring the center-to-center distance $(\bar{X}_2 - \bar{X}_1)_{\text{cont}}$ upon contact, one can determine the distance upon contact $L_0 = (\bar{X}_2 - \bar{X}_1)_{\text{cont}} - (R_1 + R_2)$ thus providing information on the scale of the highest peaks of the rough silica surfaces [116].

Averaging over three contact events, we find $L_0 = (0.2 \pm 0.1) \mu\text{m}$. Such value is compatible with the estimation for the highest asperities based on the SEM images discussed in Appendix C 1. The total experimental error is determined by the error of $R_1 + R_2$ only, as the uncertainty of the center-to-center distance upon contact is much smaller.

The high peaks associated to the distance upon contact are usually sparse and thus provide a small correction to the Casimir interaction in the distance range probed in our experiments [114]. Given our limited experimental precision, we have neglected the contribution of such rare peaks.

APPENDIX D: POSITION DETECTION

We measure the position of the microsphere center by employing the edge detection algorithm of Refs. [86,87]. This method is particularly suitable when considering two microspheres at close distance, since it allows to exclude the region where the images of the microspheres overlap, producing a nontrivial diffraction pattern. Hence we determine the microsphere edge only within the region indicated by the green contour shown in Fig. 1(c). The yellow dots indicate the positions used to fit a circumference, whose center is identified as the position of the trapped microsphere. An analogous procedure is implemented for the microsphere adhered to the coverslip.

To test the precision of the position detection method, a silica microsphere of nominal radius $\bar{R} = 10 \mu\text{m}$ is attached to the coverslip and then displaced by nominal steps of 5 nm every 2 s by employing a piezoelectric nanopositioning system to drive the microscope stage along the x direction (see Appendix A for details). In Fig. 7, we plot the variation of the microsphere position with time. The averaged standard deviation for the steps shown in the figure is $(0.80 \pm 0.04) \text{ nm}$, proving our ability to detect nanometric displacements on the xy plane. The average separation between consecutive steps is $(5.4 \pm 0.2) \text{ nm}$. We also validate our position detection method by comparing results for the optical trap stiffness from three different methods: position fluctuations, Stokes

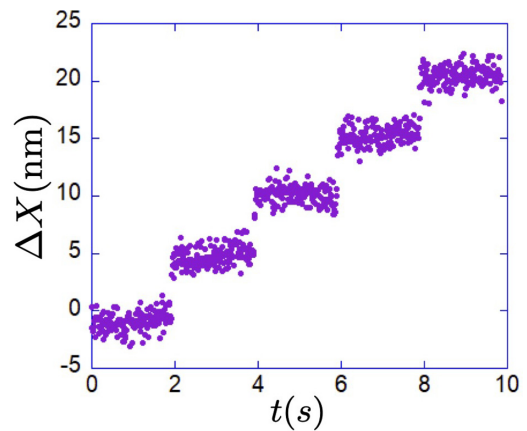


FIG. 7. Microsphere position versus time. A silica microsphere is adhered to the cover slip, which is driven laterally by 5 nm every 2 s with the help of a piezoelectric nanopositioning system.

calibration and modeling based on the Mie-Debye theory of optical tweezers [117] as discussed in Appendix E 3.

APPENDIX E: ENVIRONMENTAL NOISE

Both the stiffness calibration and the interaction measurements critically depend on the assumption of thermal equilibrium [33,90,118]. Environmental noise such as air-currents, temperature gradients, mechanical vibrations, drifts on the laser and on the microscope stage can easily drive the system far out of thermal equilibrium, creating awkward systematic measurement artifacts. For instance, extra fluctuations on the trapped microsphere are responsible for trap stiffness underestimation; directional drifts can change the relative position of both optically trapped and attached microspheres, drastically changing the interaction among them. As a result, carrying out careful experimental preparation, environmental noise characterization and mitigation actions are crucial to guarantee a thermally limited system leading to accurate stiffness calibration and interaction measurements.

Let us address each of the environmental noise sources and the actions which have been taken to mitigate them. Air currents and temperature gradients are reduced by symmetrically positioning the air conditioners in the laboratory room, and more importantly covering all the laser optical path, all the optical devices and the optical microscope with a home-made enclosure made of cardboard with a few layers of bubblewrap foil. Mechanical noise is reduced by mounting all of the optical elements in small optical posts attached on an optical breadboard placed on a conventional optical table as discussed in Appendix A.

1. Laser drift

Laser drifting is cautiously characterized during all interaction experiments. Figure 8(a) shows the long time dependence (temporal scale of \sim hours) of the position deviation Δx from the average initial position of the optically trapped microsphere, when no salt was added to the solution (see Sec. III A). Each dot represents the mean position of the optically trapped microsphere over an experimental run of $\mathcal{T} = 500 \text{ s}$, with

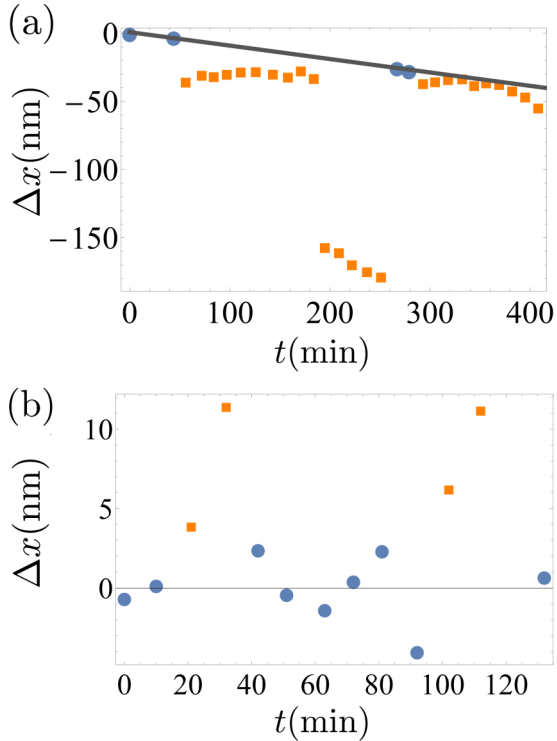


FIG. 8. (a) Center of mass position deviation Δx of the optically trapped microsphere as a function of time for the experimental runs with (a) low and (b) high salt concentrations. Blue data points correspond to the situation with no interaction (large distance D), while orange ones represent the position deviation in the presence of colloidal interactions. The solid line in (a) is a linear fit of the blue points indicating a laser drift of ~ 0.1 nm/min.

the exposure time $W = 2$ ms. The blue dots correspond to the situation with no interaction as the average separation between the microspheres is large: $L \gtrsim 500$ nm (see Fig. 1 of the main text). On the other hand, the orange plateaus correspond to distances $L < 400$ nm such that the interaction is non-negligible. The figure shows that as the microspheres are moved closer and further away, the optically trapped microsphere has not returned back to its original position, being slowly carried by a laser drift. Repeating this back and forth protocol and fitting a straight line to the set of isolation points, we find a laser drift of ~ 0.1 nm/min, which was used as a correction for the unperturbed equilibrium position $L_{\text{eq}}^{\text{opt}}$ (see section III A) in the experiment with low salt concentration.

In Fig. 8(b), Δx as a function of time is shown for the experiment with high salt concentration (see Sec. III B). In the case of interaction (orange points), the position deviations are along the positive x axis, indicating attraction as expected [see Fig. 1(a)]. In contrast to the low-concentration experiment shown in Fig. 8(a), here no substantial laser drift takes place, as indicated by the blue dots corresponding to large distances $L \gtrsim 500$ nm. We hypothesize that this behavior is due to different environmental conditions between the two experimental rounds, since they were conducted on distinct days. As indicated by Fig. 8(b), the blue dots are scattered around zero with a standard deviation $\sigma_{\text{drift}} \sim 2$ nm, which allows us to estimate the experimental error in our force interaction

measurements. For a trap stiffness $k \sim 1$ fN/nm, we then have a force error $\delta F \approx k\sigma_{\text{drift}} \sim 2$ fN, which is shown in Fig. 4 as a shaded region and also represents the minimum detectable interaction force of our experimental setup.

2. Microscope stage drift

Microscope stage drifts were mitigated by active control stabilization using a feedback loop [119] simultaneously in the three x , y , and z axis. As shown in Fig. 1(b) and described in Sec. A, the attached microsphere's position is continuously monitored by a CCD camera taking position measurements at a sampling rate of 32 fps and averaging over 20 frames, thus giving an effective sampling rate of $r_{\text{feed}} = 1.6$ fps. Each measurement is then returned back as a feedback signal to the digital piezoelectric controller, which performs the position corrections, thus enabling to keep the position variations along the three axes below 10 nm for each experimental run of 500 s.

3. Trap stiffness calibration

Stiffness calibration is carried out by applying the two well-known methods of potential energy fitting [91,118,120] and drag force counterbalance [118,121]. In the former protocol, which is entirely based on thermal fluctuations analysis [122–124], the energy potential landscape of an optically trapped microsphere is constructed by monitoring the diffusive Brownian motion of the microsphere along the y direction, which is orthogonal to the interaction force as indicated by Fig. 1(c). The corresponding trap stiffness is then obtained by fitting a quadratic function to the potential energy. In the latter protocol, the optically trapped microsphere experiences a viscous drag force by creating a fluid flowing in its surroundings. By counterbalancing that hydrodynamical force, which is described by the Stokes-Faxén law [33,125–127], to the optical tweezers' restoring force, the desired stiffness along the direction of the fluid flow is obtained.

In Fig. 9, we plot the trap stiffness as a function of the laser power P at the objective entrance port. We show the results from the two calibration protocols in the same plot. Each protocol is employed for an individual silica microsphere (nominal radius $\bar{R}_1 = 2.5$ μm) from the same batch (see Appendix B for details). The size dispersion within a given batch is negligible, so we expect the results for the two measured microspheres to agree within error bars. The black dots are the trap stiffness k_y along the y axis obtained from the analysis of the Brownian motion of the optically trapped microsphere in actual interaction measurement runs. This motion is monitored with an exposure time of $W = 2$ ms and with a sampling rate of $f_s = 10$ fps. Since the correlation time of Brownian fluctuations in the optical trap is $\tau_c \sim 100$ ms, those values for W and f_s respectively avoid motion blur corrections [90,128] and correlated data [129]. Fitting a linear function crossing the origin to the set of calibration points gives the angular coefficient $k_y/P = (0.129 \pm 0.001)$ fN nm $^{-1}$ mW $^{-1}$, where the uncertainty is obtained from the weighted fitting procedure.

The blue dots in Fig. 9 are the results for the trap stiffness k_x along the x axis obtained by the drag force calibration method. They are acquired with $W = 2.8$ ms and $f_s = 357$ fps, which guarantee proper relaxation and counterbalance

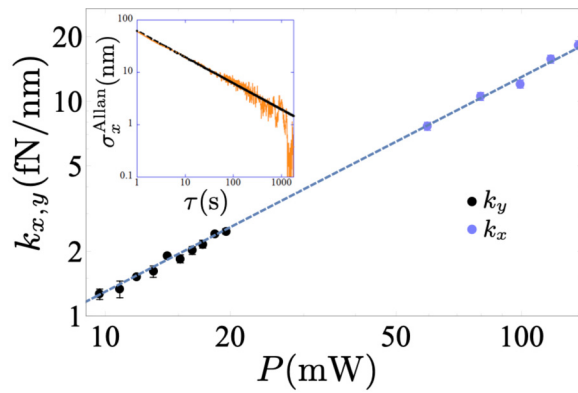


FIG. 9. Optical tweezers' stiffnesses k_x (blue dots) and k_y (black dots) versus laser power P at the objective entrance port. k_x and k_y are measured by the drag force and fluctuation methods, respectively. While k_x is measured for an isolated microsphere, k_y is obtained from the fluctuations in actual interaction measurement runs. We find the same angular coefficient when fitting the two sets of data points separately, which also agrees with an independent theoretical calculation. The resulting best fit (dashed line) indicates the equivalence between the two calibration protocols, as well as the isotropy of the optical force field on the xy plane as expected for circular polarization. Inset: Allan deviation of an isolated optically trapped microsphere's x position as function of time. The dashed line represents the thermal limit deviation showing that the system is thermally limited along the whole time interval until $\tau \sim 1000$ s.

monitoring. The corresponding weighted linear fit to this calibration set yields the angular coefficient $k_x/P = (0.129 \pm 0.003) \text{ fN nm}^{-1} \text{ mW}^{-1}$, which is in excellent agreement with the value obtained for k_y/P from Brownian fluctuations. For convenience, we have employed circularly polarized trapping beams in all experiments reported in this paper. Thus we expect the optical trap stiffness to be the same along all directions on the xy plane, also because the effect of residual astigmatism on the optical force field is negligible in this size range [130,131]. Indeed, isotropy of the optical force field on the xy plane allows us to use the Brownian fluctuations along the y direction, which is orthogonal to the interaction force between the two microspheres, as a check of the optical force during the interaction runs. The dashed straight line shown in Fig. 9, corresponding to the best fit linear function, provides further visual indication of the compatibility between the two calibrations protocols performed along the orthogonal x and y axis.

As a third method, we have employed the Mie-Debye theory of optical tweezers [117] to calculate the optical trap stiffness. Such absolute calibration method [130,131] also relies on an independent characterization of all input parameters required by the theoretical model: the objective transmittance, beam waist at the objective entrance port, microsphere radius, and refractive indexes of the microsphere and host medium. In addition, the known values for the laser wavelength, objective numerical aperture and focal length ($f = 4.44$ mm) are also required (see Appendix A).

To determine the laser power at the sample region, the objective transmittance is characterized as in Ref. [132]: a laser beam, with the same waist employed in the trapping experiment, is transmitted through the water-immersion objective

and then reflected back into the objective by a mirror attached to the microscope stage. We found a single-pass transmittance of 0.55 ± 0.06 . The method of Ref. [132] also allows for the characterization of the beam waist w at the objective entrance port. We found $w = 2.34$ mm.

We measured the radius of the trapped silica microspheres from SEM images and found $R_1 = (2.35 \pm 0.02) \mu\text{m}$ with negligible size dispersion within our batch as discussed in Appendix C 1. Two independent methods were recently employed to measure the refractive index of silica microspheres from the same batch at $\lambda_0 = 470$ nm [85]. The result is smaller than the bulk fused silica index, which we attribute to the porosity of the beads (see also [133] for related findings from a mass measurement). In order to infer the refractive index at the trapping laser wavelength $\lambda_0 = 1064$ nm, we employ the (Mie-based) extended Maxwell-Garnett (EMG) effective medium theory [134,135] assuming that our silica beads are filled with empty pores. From the refractive index measured at 470 nm, we obtain a volume filling fraction 0.078, which we then employ to calculate $n_{\text{bead}} = 1.4146 \pm 0.0019$ from the bulk fused silica refractive index $n_{\text{silica}} = 1.4496$ at $\lambda_0 = 1064$ nm [136] by employing again the EMG theory. At this wavelength of interest, the refractive index of distilled water at 24°C is $n_{\text{water}} = 1.3242$ [137]. We take this value as the refractive index of the host medium, since its modification for a salt concentration of ~ 0.2 mM (see Sec. III A) is negligible ($\Delta n \sim 10^{-5}$ according to Ref. [138]).

We assume that optical effects of refraction at the planar interface between the glass slide and the sample region are canceled when using the water-immersion objective (see Appendix A). Most importantly, the spherical aberration introduced by the interface, which might lead to a strong reduction of the trap stiffness [139], is corrected by the water-immersion objective. We disregard modifications due to a possible small astigmatism of the trapping beam, which are typically unimportant for radii $R > \lambda_0$ [130,131]. Finally, we also neglect the optical reverberation between the microsphere and the glass slide [92] given the large distance ($\approx 10 \mu\text{m}$) between the trapped particle and the slide. We then find $k_x/P = k_y/P = (0.124 \pm 0.018) \text{ fN nm}^{-1} \text{ mW}^{-1}$, in very good agreement with the measurements discussed above. Here, approximately 80% of the theoretical error originates from the objective transmittance measurement, with the refractive index of silica and radius uncertainties accounting for the rest.

Overall, the agreement between the three different calibration methods provides further validation of our detection method and indicates that nonthermal fluctuations in our system are negligible given the precision of our measurements. The latter is an essential requirement for probing the interaction potential from the microsphere position fluctuations. We provide additional evidence that our system is thermally limited by analyzing the Allan deviation in the next sub-section.

4. Allan deviation stability analysis

A successful Brownian stiffness calibration already indicates that the motion of the optically trapped microsphere is thermally limited. However, it is also important to determine the optimal time over which it remains in that state, i.e., in the absence of any extra nonthermal fluctuations and drifts. One

way to quantify this stabilization time is performing an Allan-deviation stability analysis [46,140–143]. The Allan deviation of the position of the optically trapped microsphere along the x axis is defined as

$$\sigma_x^{\text{Allan}}(\tau) = \left\{ \frac{1}{A-1} \sum_{j=1}^{A-1} \frac{1}{2} [\langle x_{j+1} \rangle(\tau) - \langle x_j \rangle(\tau)]^2 \right\}^{1/2}, \quad (\text{E1})$$

where $A = \mathcal{T}/\tau$ is the number of independent length- τ blocks in a run of total duration \mathcal{T} . The j th bin average $\langle x_j \rangle(\tau)$ is taken over the interval $[(j-1)\tau, j\tau]$ with $f_s\tau$ points, where f_s is the sampling rate. The Allan deviation measures the average position variation among consecutive temporal intervals of length τ . In the absence of nonthermal noise, the longer the interval τ , the closer the averages in consecutive intervals will be, thus gradually decreasing the Allan deviation with increasing τ .

In the inset of Fig. 9, we plot the Allan deviation $\sigma_x^{\text{Allan}}(\tau)$ versus time τ for an optically trapped microsphere under the environmental conditions corresponding to the Casimir measurement with high salt concentration [see Fig. 8(b)]. The surface-to-surface distance is $L \sim 800$ nm, the total time duration is $\mathcal{T} = 3200$ s and the sampling rate is $f_s = 1$ Hz. The dashed line shows the thermal limit deviation $\sigma_{\text{Th}}^{\text{Allan}}(\tau) = \sqrt{2\gamma k_B T / k_x^2 \tau}$ [141], where all parameters are determined independently of the Allan deviation analysis, with no fitting procedure. We take $k_x = 1$ fN/nm, obtained from the calibration procedure described in the previous sub-section, the Stokes friction coefficient $\gamma = 5 \times 10^{-7}$ kg/s corrected for the proximity to the coverslip [127], and the measured temperature $T = (296 \pm 1)$ K. The blind comparison between the experimental results and $\sigma_{\text{Th}}^{\text{Allan}}(\tau)$ shows that our system is stable and thermally limited out to ≈ 1000 s, approximately twice the time interval of all experimental calibration and interaction runs. For times $\tau \gtrsim 1000$ s, lack of statistics hinders any analysis.

-
- [1] J. N. Israelachvili, *Intermolecular and Surface Forces* (Academic Press, Waltham, 2011).
- [2] H. J. Butt and M. Kappl, *Surface and Interfacial Forces* (Wiley-VCH, Weinheim, 2010).
- [3] E. M. Lifshitz, The theory of molecular attractive forces between solids, *Sov. Phys. JETP* **2**, 73 (1956).
- [4] I. E. Dzyaloshinskii, E. M. Lifshitz, and L. P. Pitaevskii, The general theory of van der Waals forces, *Adv. Phys.* **10**, 165 (1961).
- [5] W. B. Russel, D. A. Saville, and W. R. Schowalter, *Colloidal Dispersions* (Cambridge University Press, New York, 1989).
- [6] H. B. G. Casimir, On the attraction between two perfectly conducting plates, *Proc. K. Ned. Akad. Wet.* **51**, 793 (1948).
- [7] S. K. Lamoreaux, Demonstration of the Casimir Force in the 0.6 to 6 μm Range, *Phys. Rev. Lett.* **78**, 5 (1997).
- [8] U. Mohideen and A. Roy, Precision Measurement of the Casimir Force from 0.1 to 0.9 μm , *Phys. Rev. Lett.* **81**, 4549 (1998).
- [9] H. B. Chan, V. A. Aksyuka, R. N. Kleiman, D. J. Bishop, and F. Capasso, Quantum mechanical actuation of microelectromechanical systems by the Casimir force, *Science* **291**, 1941 (2001).
- [10] R. S. Decca, D. López, E. Fischbach, G. L. Klimchitskaya, D. E. Krause, and V. M. Mostepanenko, Tests of new physics from precise measurements of the Casimir pressure between two gold-coated plates, *Phys. Rev. D* **75**, 077101 (2007).
- [11] A. O. Sushkov, W. J. Kim, D. A. R. Dalvit, and S. K. Lamoreaux, Observation of the thermal Casimir force, *Nat. Phys.* **7**, 230 (2011).
- [12] C.-C. Chang, A. A. Banishev, R. Castillo-Garza, G. L. Klimchitskaya, V. M. Mostepanenko, and U. Mohideen, Gradient of the Casimir force between Au surfaces of a sphere and a plate measured using an atomic force microscope in a frequency-shift technique, *Phys. Rev. B* **85**, 165443 (2012).
- [13] G. Bimonte, D. López, and R. S. Decca, Isoelectronic determination of the thermal Casimir force, *Phys. Rev. B* **93**, 184434 (2016).
- [14] M. Liu, J. Xu, G. L. Klimchitskaya, V. M. Mostepanenko, and U. Mohideen, Precision measurements of the gradient of the Casimir force between ultraclean metallic surfaces at larger separations, *Phys. Rev. A* **100**, 052511 (2019).
- [15] G. Bimonte, B. Spreng, P. A. Maia Neto, G.-L. Ingold, G. L. Klimchitskaya, V. M. Mostepanenko, and R. Decca, Measurement of the Casimir force between 0.2 and 8 μm : Experimental procedures and comparison with theory, *Universe* **7**, 93 (2021).
- [16] S. de Man, K. Heeck, R. J. Wijngaarden, and D. Iannuzzi, Halving the Casimir Force with Conductive Oxides, *Phys. Rev. Lett.* **103**, 040402 (2009).
- [17] J. L. Garrett, D. A. T. Somers, and J. N. Munday, Measurement of the Casimir Force between Two Spheres, *Phys. Rev. Lett.* **120**, 040401 (2018).
- [18] G. L. Klimchitskaya and V. M. Mostepanenko, Recent measurements of the Casimir force: Comparison between experiment and theory, *Mod. Phys. Lett. A* **35**, 2040007 (2020).
- [19] T. Gong, M. R. Corrado, A. R. Mahbub, C. Shelden, and J. N. Munday, Recent progress in engineering the Casimir effect – applications to nanophotonics, nanomechanics, and chemistry, *Nanophotonics* **10**, 523 (2021).
- [20] L. M. Woods, D. A. R. Dalvit, A. Tkatchenko, P. Rodriguez-Lopez, A. W. Rodriguez, and R. Podgornik, Materials perspective on Casimir and van der Waals interactions, *Rev. Mod. Phys.* **88**, 045003 (2016).
- [21] P. A. Maia Neto, F. S. S. Rosa, L. B. Pires, A. Moraes, A. Canaguier-Durand, R. Guérout, A. Lambrecht, and S. Reynaud, Scattering theory of the screened Casimir interaction in electrolytes, *Eur. Phys. J. D* **73**, 178 (2019).
- [22] H. I. Petrache, T. Zemb, L. Belloni, and V. A. Parsegian, Salt screening and specific ion adsorption determine neutral-lipid membrane interactions, *Proc. Natl. Acad. Sci. U.S.A.* **103**, 7982 (2006).
- [23] A. Ashkin, J. M. Dziedzic, J. E. Bjorkholm, and S. Chu, Observation of a single-beam gradient force optical trap for dielectric particles, *Opt. Lett.* **11**, 288 (1986).

- [24] A. Ashkin, *Optical Trapping and Manipulation of Neutral Particles Using Lasers: A Reprint Volume With Commentaries* (World Scientific, Singapore, 2006).
- [25] A. Gennerich (ed.), *Optical Tweezers Methods and Protocols* (Humana Press, New York, 2017).
- [26] J. N. Munday and F. Capasso, Precision measurement of the Casimir-Lifshitz force in a fluid, *Phys. Rev. A* **75**, 060102(R) (2007).
- [27] J. N. Munday, F. Capasso, V. A. Parsegian, and S. M. Bezrukov, Measurements of the Casimir-Lifshitz force in fluids: The effect of electrostatic forces and Debye screening, *Phys. Rev. A* **78**, 032109(R) (2008).
- [28] J. N. Munday, F. Capasso, and V. A. Parsegian, Measured long-range repulsive Casimir-Lifshitz forces, *Nature (London)* **457**, 170 (2009).
- [29] P. J. van Zwol and G. Palasantzas, Repulsive Casimir forces between solid materials with high-refractive-index intervening liquids, *Phys. Rev. A* **81**, 062502 (2010).
- [30] A. Le Cunuder, A. Petrosyan, G. Palasantzas, V. Svetovoy, and S. Ciliberto, Measurement of the Casimir force in a gas and in a liquid, *Phys. Rev. B* **98**, 201408(R) (2018).
- [31] V. A. Parsegian and B. W. Ninham, Toward the correct calculation of van der Waals interactions between lyophobic colloids in an aqueous medium, *J. Colloid Interface Sci.* **37**, 332 (1971).
- [32] A. Ashkin, Forces of a single-beam gradient laser trap on a dielectric sphere in the ray optics regime, *Biophys. J.* **61**, 569 (1992).
- [33] E. Schäffer, S. F. Nørrelykke, and J. Howard, Surface forces and drag coefficients of microspheres near a plane surface measured with optical tweezers, *Langmuir* **23**, 3654 (2007).
- [34] C. Gutsche, U. F. Keyser, K. Kegler, F. Kremer, and P. Linse, Forces between single pairs of charged colloids in aqueous salt solutions, *Phys. Rev. E* **76**, 031403 (2007).
- [35] M. M. Elmahdy, C. Gutsche, and F. Kremer, Forces within single pairs of charged colloids in aqueous solutions of ionic liquids as studied by optical tweezers, *J. Phys. Chem. C* **114**, 19452 (2010).
- [36] G. Dominguez-Espinosa, A. Synytska, A. Drechsler, C. Gutsche, K. Kegler, P. Uhlmann, M. Stamm, and F. Kremer, Optical tweezers to measure the interaction between poly(acrylic acid) brushes, *Polymer* **49**, 4802 (2008).
- [37] P. M. Hansen, J. K. Dreyer, J. Ferkinghoff-Borg, and L. Oddershede, Novel optical and statistical methods reveal colloid-wall interactions inconsistent with DLVO and Lifshitz theories, *J. Colloid Interface Sci.* **287**, 561 (2005).
- [38] D. S. Ether, L. B. Pires, S. Umrath, D. Martinez, Y. Ayala, B. Pontes, G. R. S. Araújo, S. Frases, G.-L. Ingold, F. S. S. Rosa, N. B. Viana, H. M. Nussenzveig, and P. A. Maia Neto, Probing the Casimir force with optical tweezers, *Europhys. Lett.* **112**, 44001 (2015).
- [39] A. Kundu, S. Paul, S. Banerjee, and A. Banerjee, Measurement of van der Waals force using oscillating optical tweezers, *Appl. Phys. Lett.* **115**, 123701 (2019).
- [40] S. Paladugu, A. Callegari, Y. Tuna, L. Barth, S. Dietrich, A. Gambassi, and G. Volpe, Nonadditivity of critical Casimir forces, *Nat. Commun.* **7**, 1 (2016).
- [41] J. C. Crocker and D. G. Grier, Microscopic Measurement of the Pair Interaction Potential of Charge-Stabilized Colloid, *Phys. Rev. Lett.* **73**, 352 (1994).
- [42] D. G. Grier, Optical tweezers in colloid and interface science, *Curr. Opin. Colloid Interface Sci.* **2**, 264 (1997).
- [43] S. K. Sainis, V. Germain, and E. R. Dufresne, Statistics of Particle Trajectories at Short Time Intervals Reveal fN-Scale Colloidal Forces, *Phys. Rev. Lett.* **99**, 018303 (2007).
- [44] S. K. Sainis, C. O. Mejean V. Germain, and E. R. Dufresne, Electrostatic interactions of colloidal particles in nonpolar solvents: Role of surface chemistry and charge control agents, *Langmuir* **24**, 1160 (2008).
- [45] M. Polin, D. G. Grier, and Y. Han, Colloidal electrostatic interactions near a conducting surface, *Phys. Rev. E* **76**, 041406 (2007).
- [46] G. Schnoering, Y. Rosales-Cabara, H. Wendehenne, A. Canaguier-Durand, and C. Genet, Thermally Limited Force Microscopy on Optically Trapped Single Metallic Nanoparticles, *Phys. Rev. Appl.* **11**, 034023 (2019).
- [47] D. C. Prieve, S. G. Bike, and N. A. Frej, Brownian motion of a single microscopic sphere in a colloidal force field, *Faraday Discuss. Chem. Soc.* **90**, 209 (1990).
- [48] L. Liu, S. Kheifets, V. Ginis, and F. Capasso, Subfemtonewton Force Spectroscopy at the Thermal Limit in Liquids, *Phys. Rev. Lett.* **116**, 228001 (2016).
- [49] L. Liu, A. Woolf, A. W. Rodriguez, and F. Capasso, Absolute position total internal reflection microscopy with an optical tweezer, *Proc. Natl. Acad. Sci. U.S.A.* **111**, E5609 (2014).
- [50] C. Hertlein, L. Helden, A. Gambassi, S. Dietrich, and C. Bechinger, Direct measurement of critical Casimir forces, *Nature (London)* **451**, 172 (2008).
- [51] M. A. Bevan and D. C. Prieve, Direct measurement of retarded van der Waals attraction, *Langmuir* **15**, 7925 (1999).
- [52] M. Nayeri, Z. Abbas, and J. Bergenholtz, Measurements of screening length in salt solutions by total internal reflection microscopy: Influence of van der Waals forces and instrumental noise, *Colloids Surf. A: Physicochem. Eng. Asp.* **429**, 74 (2013).
- [53] F. Cao, W. Jiahao, L. Yunxing, and T. Ngai, Measurements of particle surface interactions in both equilibrium and nonequilibrium systems, *Langmuir* **35**, 8910 (2019).
- [54] A. M. Smith, M. Borkovec, and G. Trefalt, Forces between solid surfaces in aqueous electrolyte solutions, *Adv. Colloid Interface Sci.* **275**, 102078 (2020).
- [55] M. Elzbiaciak-Wodka, M. N. Popescu, F. J. M. Ruiz-Cabello, G. Trefalt, P. Maroni, and M. Borkovec, Measurements of dispersion forces between colloidal latex particles with the atomic force microscope and comparison with Lifshitz theory, *J. Chem. Phys.* **140**, 104906 (2014).
- [56] D. J. Mitchell and P. Richmond, A general formalism for the calculation of free energies of inhomogeneous dielectric and electrolytic systems, *J. Colloid Interface Sci.* **46**, 118 (1974).
- [57] J. Mahanty and B. W. Ninham, *Dispersion Forces* (Academic Press, London, 1976).
- [58] V. A. Parsegian, *Van der Waals Forces: A Handbook for Biologists, Chemists, Engineers, and Physicists* (Cambridge University Press, New York, 2005).
- [59] M. T. Jaekel and S. Reynaud, Casimir force between partially transmitting mirrors, *J. Phys. I (France)* **1**, 1395 (1991).
- [60] C. Genet, A. Lambrecht, and S. Reynaud, Casimir force and the quantum theory of lossy optical cavities, *Phys. Rev. A* **67**, 043811 (2003).

- [61] B. Davies and B. W. Ninham, Van der Waals forces in electrolytes, *J. Chem. Phys.* **56**, 5797 (1972).
- [62] S. H. Donaldson, Jr., A. Royne, K. Kristiansen, M. V. Rapp, S. Das, M. A. Gebbie, D. W. Lee, P. Stock, M. Valtiner, and J. Israelachvili, Developing a general interaction potential for hydrophobic and hydrophilic interactions, *Langmuir* **31**, 2051 (2015).
- [63] G. M. Bell, S. Levine, and L. N. McCartney, Approximate methods of determining the double-layer free energy of interaction between two charged colloidal spheres, *J. Colloid Interface Sci.* **33**, 335 (1970).
- [64] D. S. Ether, F. S. S. Rosa, D. M. Tibaduiza, L. B. Pires, R. S. Decca, and P. A. Maia Neto, Double-layer force suppression between charged microspheres, *Phys. Rev. E* **97**, 022611 (2018).
- [65] S. L. Carnie and D. Y. C. Chan, Interaction free energy between identical spherical colloidal particles: The linearized Poisson-Boltzmann theory, *J. Colloid Interface Sci.* **155**, 297 (1993).
- [66] G. Trefalt, S. H. Behrens, and M. Borkovec, Charge regulation in the electrical double layer: Ion adsorption and surface interactions, *Langmuir* **32**, 380 (2016).
- [67] S. L. Carnie, D. Y. C. Chan, and J. S. Gunning, Electrical double layer interaction between dissimilar spherical colloidal particles and between a sphere and a plate: The linearized Poisson-Boltzmann theory, *Langmuir* **10**, 2993 (1994).
- [68] A. Lambrecht, P. A. Maia Neto, and S. Reynaud, The Casimir effect within scattering theory, *New J. Phys.* **8**, 243 (2006).
- [69] S. J. Rahi, T. Emig, N. Graham, R. L. Jaffe, and M. Kardar, Scattering theory approach to electrodynamic Casimir forces, *Phys. Rev. D* **80**, 085021 (2009).
- [70] T. Emig, N. Graham, R. L. Jaffe, and M. Kardar, Casimir Forces between Arbitrary Compact Objects, *Phys. Rev. Lett.* **99**, 170403 (2007).
- [71] P. A. Maia Neto, A. Lambrecht, and S. Reynaud, Casimir energy between a plane and a sphere in electromagnetic vacuum, *Phys. Rev. A* **78**, 012115 (2008).
- [72] A. Canaguier-Durand, P. A. Maia Neto, A. Lambrecht, and S. Reynaud, Thermal Casimir Effect in the Plane-Sphere Geometry, *Phys. Rev. Lett.* **104**, 040403 (2010).
- [73] P. Rodriguez-Lopez, Casimir energy and entropy in the sphere-sphere geometry, *Phys. Rev. B* **84**, 075431 (2011).
- [74] B. Spreng, P. A. Maia Neto, and G.-L. Ingold, Plane-wave approach to the exact van der Waals interaction between colloid particles, *J. Chem. Phys.* **153**, 024115 (2020).
- [75] B. Derjaguin, Untersuchungen über die Reibung und Adhäsion, IV – Theorie des Anhaftens kleiner Teilchen, *Kolloid-Zs.* **69**, 155 (1934).
- [76] T. Emig, Fluctuation-induced quantum interactions between compact objects and a plane mirror, *J. Stat. Mech.* (2008) P04007.
- [77] L. P. Teo, M. Bordag, and V. Nikolaev, Corrections beyond the proximity force approximation, *Phys. Rev. D* **84**, 125037 (2011).
- [78] G. Bimonte and T. Emig, Exact Results for Classical Casimir Interactions: Dirichlet and Drude Model in the Sphere-Sphere and Sphere-Plane Geometry, *Phys. Rev. Lett.* **109**, 160403 (2012).
- [79] G. Bimonte, T. Emig, R. L. Jaffe, and M. Kardar, Casimir forces beyond the proximity approximation, *Europhys. Lett.* **97**, 50001 (2012).
- [80] M. Hartmann, G.-L. Ingold, and P. A. Maia Neto, Plasma Versus Drude Modeling of the Casimir Force: Beyond the Proximity Force Approximation, *Phys. Rev. Lett.* **119**, 043901 (2017).
- [81] G. Bimonte, Beyond-proximity-force-approximation Casimir force between two spheres at finite temperature. II. Plasma versus Drude modeling, grounded versus isolated spheres, *Phys. Rev. D* **98**, 105004 (2018).
- [82] V. Henning, B. Spreng, M. Hartmann, G.-L. Ingold, and P. A. Maia Neto, The role of diffraction in the Casimir effect beyond the proximity force approximation, *J. Opt. Soc. Am. B* **36**, C77 (2019).
- [83] R. O. Nunes, B. Spreng, R. de Melo e Souza, G.-L. Ingold, P. A. Maia Neto, and F. S. S. Rosa, The Casimir interaction between spheres immersed in electrolytes, *Universe* **7**, 156 (2021).
- [84] U. Agero, C. H. Monken, C. Ropert, R. T. Gazzinelli, and O. N. Mesquita, Cell surface fluctuations studied with defocusing microscopy, *Phys. Rev. E* **67**, 051904 (2003).
- [85] F. Gómez, R. S. Dutra, L. B. Pires, G. R. S. Araújo, B. Pontes, P. A. Maia Neto, H. M. Nussenzveig, and N. B. Viana, Non-Paraxial Mie Theory of Image Formation in Optical Microscopes and Characterization of Colloidal Particles, *Phys. Rev. Appl.* **15**, 064012 (2021).
- [86] O. Ueberschär, C. Wagner, T. Stangner, C. Gutsche, and F. Kremer, A novel video-based microsphere localization algorithm for low contrast silica particles under white light illumination, *Opt. Lasers Eng.* **50**, 423 (2012).
- [87] H. Yücel and N. T. Okumuşoğlu, A new tracking algorithm for multiple colloidal particles close to contact, *J. Phys.: Condens. Matter* **29**, 465101 (2017).
- [88] M. D. A. Cooley and M. E. O'Neill, On the slow motion generated in a viscous fluid by the approach of a sphere to a plane wall or stationary sphere, *Mathematika* **16**, 37 (1969).
- [89] H. Faxén, Der Widerstand gegen die Bewegung einer starren Kugel in einer zähen Flüssigkeit, die zwischen zwei parallelen ebenen Wänden eingeschlossen ist, *Ann. Phys. (Leipzig)* **373**, 89 (1922).
- [90] W. P. Wong and K. Halvorsen, The effect of integration time on fluctuation measurements: calibrating an optical trap in the presence of motion blur, *Opt. Express* **14**, 12517 (2006).
- [91] E.-L. Florin, A. Pralle, E. H. K. Stelzer, and J. K. H. Hörber, Photonic force microscope calibration by thermal noise analysis, *Appl. Phys. A* **66**, S75 (1998).
- [92] R. S. Dutra, P. A. Maia Neto, H. M. Nussenzveig, and H. Flyvbjerg, Theory of optical-tweezers forces near a plane interface, *Phys. Rev. A* **94**, 053848 (2016).
- [93] T. Schoger and G.-L. Ingold (private communication).
- [94] For the specific pair of runs shown in the inset of Fig. 2, it is more convenient for clarity to define the relative potential offset by taking $L_{\text{ref}} = 0.40 \mu\text{m}$, since the distances are larger than those shown in the main plot.
- [95] S. H. Behrens and D. G. Grier, The charge of glass and silica surfaces, *J. Chem. Phys.* **115**, 6716 (2001).
- [96] B. Spreng, M. Hartmann, V. Henning, P. A. Maia Neto, and G.-L. Ingold, Proximity force approximation and specular

- reflection: Application of the WKB limit of Mie scattering to the Casimir effect, *Phys. Rev. A* **97**, 062504 (2018).
- [97] B. Liu, B. Poolman, and A. J. Boersma, Ionic strength sensing in living cells, *ACS Chem. Biol.* **12**, 2510 (2017).
- [98] C. L. Fonta and B. M. Humbel, Correlative microscopy, *Arch. Biochem. Biophys.* **581**, 98 (2015).
- [99] T. Ando, S. P. Bhamidimarri, N. Brending, H. Colin-York, L. Collinson, N. De Jonge, P. J. de Pablo, E. Debroye, C. Eggeling, C. Franck, M. Fritzsche, H. Gerritsen, B. N. G. Giepmans, K. Grunewald, J. Hofkens, J. P. Hoogenboom, K. P. F. Janssen, R. Kaufmann, J. Klumperman, N. Kurniawan *et al.*, The 2018 correlative microscopy techniques roadmap, *J. Phys. D: Appl. Phys.* **51**, 443001 (2018).
- [100] J. L. M. J. Van Bree, J. A. Poulis, B. J. Verhaar, and K. Schram, The influence of surface irregularities upon the van der Waals forces between macroscopic bodies, *Physica* **78**, 187 (1974).
- [101] A. A. Maradudin and P. Mazur, Effects of surface roughness on the van der Waals force between macroscopic bodies, *Phys. Rev. B* **22**, 1677 (1980).
- [102] J. Czarnecki and T. Dabros, Attenuation of the van der Waals attraction energy in the particle semi-infinite medium system due to the roughness of the particle surface, *J. Colloid Interface Sci.* **78**, 25 (1980).
- [103] P. Mazur and A. A. Maradudin, Effects of surface roughness on the van der Waals force between macroscopic bodies. II. Two rough surfaces, *Phys. Rev. B* **23**, 695 (1981).
- [104] P. J. van Zwol, G. Palasantzas, and J. Th. M. De Hosson, Influence of random roughness on the Casimir force at small separations, *Phys. Rev. B* **77**, 075412 (2008).
- [105] E. Namsoon, D. F. Parsons, and V. S. J. Craig, Roughness in surface force measurements: Extension of DLVO theory to describe the forces between Hafnia surfaces, *J. Phys. Chem. B* **121**, 6442 (2017).
- [106] V. Valmacco, M. Elzbiaciak-Wodka, C. Besnard, P. Maroni, G. Trefalt, and M. Borkovec, Dispersion forces acting between silica particles across water: influence of nanoscale roughness, *Nanoscale Horiz.* **1**, 325 (2016).
- [107] M. Bordag, G. L. Klimchitskaya, and V. M. Mostepanenko, Corrections to the Casimir force between plates with stochastic surfaces, *Phys. Lett. A* **200**, 95 (1995).
- [108] G. L. Klimchitskaya and Yu. V. Pavlov, The corrections to the Casimir forces for configurations used in experiments: The spherical lens above the plane and two crossed cylinders, *Int. J. Mod. Phys. A* **11**, 3723 (1996).
- [109] G. L. Klimchitskaya, A. Roy, U. Mohideen, and V. M. Mostepanenko, Complete roughness and conductivity corrections for Casimir force measurement, *Phys. Rev. A* **60**, 3487 (1999).
- [110] C. Genet, A. Lambrecht, P. A. Maia Neto, and S. Reynaud, The Casimir force between rough metallic plates, *Europhys. Lett.* **62**, 484 (2003).
- [111] P. A. Maia Neto, A. Lambrecht, and S. Reynaud, Roughness correction to the Casimir force: Beyond the proximity force approximation, *Europhys. Lett.* **69**, 924 (2005).
- [112] P. A. Maia Neto, A. Lambrecht, and S. Reynaud, Casimir effect with rough metallic mirrors, *Phys. Rev. A* **72**, 012115 (2005).
- [113] P. A. Maia Neto, A. Lambrecht, and S. Reynaud, Roughness correction in the Casimir effect with metallic plates, *J. Phys. A: Math. Gen.* **39**, 6517 (2006).
- [114] W. Broer, G. Palasantzas, J. Knoester, and V. B. Svetovoy, Roughness correction to the Casimir force beyond perturbation theory, *Europhys. Lett.* **95**, 30001 (2011).
- [115] V. B. Svetovoy and G. Palasantzas, Influence of surface roughness on dispersion forces, *Adv. Colloid Interface Sci.* **216**, 1 (2015).
- [116] P. J. van Zwol, V. B. Svetovoy, and G. Palasantzas, Distance upon contact: Determination from roughness profile, *Phys. Rev. B* **80**, 235401 (2009).
- [117] A. Mazolli, P. A. Maia Neto, and H. M. Nussenzveig, Theory of trapping forces in optical tweezers, *Proc. R. Soc. London A* **459**, 3021 (2003).
- [118] M. P. Nicholas, L. Rao, and A. Gennerich, An improved optical tweezers assay for measuring the force generation of single kinesin molecules, *Methods Mol. Biol.* **1136**, 171 (2014).
- [119] R. McGorty, D. Kamiyama, and B. Huang, Active microscope stabilization in three dimensions using image correlation, *Opt. Nanosc.* **2**, 3 (2013).
- [120] J. Gieseler, J. R. Gomez-Solano, A. Magazzù, I. Pérez Castillo, L. Pérez García, M. Gironella-Torrent, X. Viader-Godoy, F. Ritort, G. Pesce, A. V. Arzola, K. Volke-Sepúlveda, and G. Volpe, Optical tweezers — from calibration to applications: a tutorial, *Adv. Opt. Photon.* **13**, 74 (2021).
- [121] K. C. Neuman and S. M. Block, Optical trapping, *Rev. Sci. Instrum.* **75**, 2787 (2004).
- [122] S. F. Norrelykke and H. Flyvbjerg, Power spectrum analysis with least-squares fitting: Amplitude bias and its elimination, with application to optical tweezers and atomic force microscope cantilevers, *Rev. Sci. Instrum.* **81**, 075103 (2010).
- [123] S. F. Norrelykke and H. Flyvbjerg, Harmonic oscillator in heat bath: Exact simulation of time-lapse-recorded data, exact analytical benchmark statistics, *Phys. Rev. E* **83**, 041103 (2011).
- [124] B. Melo, F. Almeida, G. Temporao, and T. Guerreiro, Relaxing constraints on data acquisition and position detection for trap stiffness calibration in optical tweezers, *Opt. Express* **28**, 16256 (2020).
- [125] K. Berg-Sorensen and H. Flyvbjerg, Power spectrum analysis for optical tweezers, *Rev. Sci. Instrum.* **75**, 594 (2004).
- [126] S. F. Tolić-Norrelykke, E. Schäffer, J. Howard, F. S. Pavone, F. Jülicher, and H. Flyvbjerg, Calibration of optical tweezers with positional detection in the back focal plane, *Rev. Sci. Instrum.* **77**, 103101 (2006).
- [127] J. Happel and H. Brenner, *Low Reynolds Number Hydrodynamics* (Martinus Nijhoff Publishers, The Hague, 1983).
- [128] A. van der Horst and N. R. Forde, Power spectral analysis for optical trap stiffness calibration from high-speed camera position detection with limited bandwidth, *Opt. Express* **18**, 7670 (2010).
- [129] H. Flyvbjerg and H. G. Petersen, Error estimates on averages of correlated data, *J. Chem. Phys.* **91**, 461 (1989).
- [130] R. S. Dutra, N. B. Viana, P. A. Maia Neto, and H. M. Nussenzveig, Absolute calibration of optical tweezers including aberrations, *Appl. Phys. Lett.* **100**, 131115 (2012).
- [131] R. S. Dutra, N. B. Viana, P. A. Maia Neto, and H. M. Nussenzveig, Absolute calibration of forces in optical tweezers, *Phys. Rev. A* **90**, 013825 (2014).
- [132] N. B. Viana, M. S. Rocha, O. N. Mesquita, A. Mazolli, and P. A. Maia Neto, Characterization of objective transmittance for optical tweezers, *Appl. Opt.* **45**, 4263 (2006).

- [133] C. P. Blakemore, A. D. Rider, S. Roy, A. Fieguth, A. Kawasaki, N. Priel, and G. Gratta, Precision Mass and Density Measurement of Individual Optically Levitated Microspheres, *Phys. Rev. Appl.* **12**, 024037 (2019).
- [134] W. T. Doyle, Optical properties of a suspension of metal spheres, *Phys. Rev. B* **39**, 9852 (1989).
- [135] R. Rupin, Evaluation of extended Maxwell-Garnett theories, *Opt. Commun.* **182**, 273 (2000).
- [136] I. H. Malitson, Interspecimen comparison of the refractive index of fused silica, *J. Opt. Soc. Am.* **55**, 1205 (1965).
- [137] M. Daimon and A. Masumura, Measurement of the refractive index of distilled water from the near-infrared region to the ultraviolet region, *Appl. Opt.* **46**, 3811 (2007).
- [138] C.-Y. Tan and Y.-X. Huang, Dependence of refractive index on concentration and temperature in electrolyte solution, polar solution, nonpolar solution, and protein solution, *J. Chem. Eng. Data* **60**, 2827 (2015).
- [139] N. B. Viana, M. S. Rocha, O. N. Mesquita, A. Mazolli, P. A. Maia Neto, and H. M. Nussenzveig, Towards absolute calibration of optical tweezers, *Phys. Rev. E* **75**, 021914 (2007).
- [140] D. W. Allan, Statistics of atomic frequency standards, *Proc. IEEE* **54**, 221 (1966).
- [141] F. Czerwinski, A. C. Richardson, and L. B. Oddershede, Quantifying noise in optical tweezers by Allan variance, *Opt. Express* **17**, 13255 (2009).
- [142] B. M. Lansdorp and O. A. Saleh, Power spectrum and Allan variance methods for calibrating single-molecule video-tracking instruments, *Rev. Sci. Instrum.* **83**, 025115 (2012).
- [143] E. Hebestreit, M. Frimmer, R. Reimann, C. Dellago, F. Ricci, and L. Novotny, Calibration and energy measurement of optically levitated nanoparticle sensors, *Rev. Sci. Instrum.* **89**, 033111 (2018).